UNIVERSITY OF CATANIA

DOCTORAL THESIS

Study of bifacial photovoltaic external operation and evaluation of energy storage through the production of hydrogen and ammonia.

Author:
Marco LEONARDI

Tutors:
Dr. Salvatore A. LOMBARDO
Prof. Maria Grazia GRIMALDI

A thesis submitted in fulfillment of the requirements
for the degree of Doctor of Philosophy

in the

Associated to CNR-IMM since 2019
February 26, 2023

Declaration of Authorship

I, Marco LEONARDI, declare that this thesis titled, “Study of bifacial photovoltaic external operation and evaluation of energy storage through the production of hydrogen and ammonia.” and the work presented in it are my own. This work was done wholly or mainly while in candidature for a research degree at this University. Where I have consulted the published work of others, this is always clearly attributed. Significant parts of the work outlined in this thesis have been published in academic journals.

- Chapter 3 is based on: **Leonardi, M.**; Corso, R.; Milazzo, R.G.; Connelli, C.; Foti, M.; Gerardi, C.; Bizzarri, F.; Privitera, S.M.S.; Lombardo, S.A. The effects of module temperature on the energy yield of bifacial photovoltaics: Data and model. *Energies* **2022**, 15, 1–14.
- Chapter 4 on: **Leonardi, M.**; Corso, R.; Scuto, A.; Milazzo, R.G.; Connelli, C.; Foti, M.; Gerardi, C.; Bizzarri, F.; Privitera, S.M.S.; Lombardo, S.A. Effects of solar spectrum and albedo on the performance of bifacial Si heterojunction mini-modules. *International 49th IEEE Photovoltaic Specialists Conference*, **2022**, Philadelphia;
- Chapter 5 on: Privitera, S.M.S.; Muller, M.; Zwaygardt, W.; Carmo, M.; Milazzo, R.G.; Zani, P.; **Leonardi, M.**; Maita, F.; Canino, A.; Foti, M.; et al. Highly efficient solar hydrogen production through the use of bifacial photovoltaics and membrane electrolysis. *J. Power Sources*, **2020**, 473, 228619.
- Chapter 6 on: Tranchida, G.; Milazzo, R.G.; **Leonardi, M.**; Scalese, S.; Pulvirenti, L.; Condorelli, G.G.; Bongiorno, C.; Lombardo, A.; and Privitera, S.M.S. Strategies to improve the catalytic activity of Fe-based catalysts for Nitrogen reduction reaction. Submitted on 04-Oct-2022, under review.

Signed: *Leonardi Marco*

Date: February 26, 2023

"We do not know what we want and yet we are responsible for what we are - that is the fact."

Jean-Paul Sartre

UNIVERSITY OF CATANIA

Department of Physics and Astronomy

Abstract

Doctor of Philosophy

Study of bifacial photovoltaic external operation and evaluation of energy storage through the production of hydrogen and ammonia.

by Marco LEONARDI

With the increase in world population and the consequent energy demand, the detrimental effects of fossil fuels and nonrenewable energy on the environment cannot be disregarded. Renewable energy systems are the way to build a sustainable and clean future that supports further economic growth. Among renewable energy sources, solar energy is the most promising because of the large flux of photons that arrive on Earth. Several photovoltaic technologies are available in the market; however, bifacial photovoltaics represent a promising technology for the future development of photovoltaics. Silicon heterojunction bifacial solar cells show the best results in terms of energy yield and power output. The first part of this dissertation covers two aspects of bifacial photovoltaic technology: the improvement of the previous mathematical model and the electrical characterization of two bifacial mini-modules operating outdoors. The main results show how the peculiar capacity of the bifacial solar cell to harvest light also by the back side grants extra power compared with the monofacial standard cell and how the environmental variables affect the electrical performance, especially temperature and solar spectral irradiance. …

The intrinsic variability of the power output of renewables requires a system for energy conversion and subsequent storage. Therefore, it is crucial to develop a process that can produce an energy vector that can convert electricity into chemicals or other forms of energy suitable for storage. Wherefore, in the second part of the dissertation, the focus is set on solar hydrogen production via proton exchange membrane electrolyser and its optimal coupling with photovoltaic systems previously discussed and on the production of ammonia via electrochemical reduction of nitrogen gas. Results confirm an excellent match between the bifacial solar module and the proton exchange membrane electrolyser in real outdoor conditions. The system has produced positive results with 4.2 gr of H_2 $h^{-1}m^{-2}$ and solar to hydrogen efficiency of 13.5 %. Finally, electrochemical nitrogen reduction has been evaluated in a water solution. For this purpose, iron-based catalysts were characterized and tested. Catalysts covered with nanoparticles exhibit a high electrochemical active area and showed excellent activity for nitrogen reduction reaction, with a faradaic efficiency of 15% and a maximum ammonia production rate of $85 \mu g mg_{cat}^{-1} h^{-1}$

Acknowledgements

I would first like to acknowledge and sincerely thank everyone in the department of chemistry and physics at Catania University, it truly has been a wonderful experience since day one. My advisors Dr Salvo Lombardo and Prof. Maria Grazia Grimaldi have been inspirational mentors and he has always encouraged me to face new and challenging problems throughout my PhD career. I want to thank Prof. Marco Balucani e la Prof. Simona Binetti for being a part of my candidacy and defence committees, they have always offered great advice and critiques. During, my PhD career I have been privileged to have worked with Dr Stefania Privitera, Dr Gabriella Milazzo, Dr Andrea Scuto, Roberto Corso, and Giuseppe Tranchida. Gabriella Milazzo has helped me both in and out of the lab and his ability to simplify complex ideas is truly inspiring. Roberto Corso has been a great friend and colleague and I want to thank him for all his scientific and nonscientific discussions. Dr Stefania Privitera was a great mentor, when I first joined the group, they taught me everything they could about electrochemistry and semiconductors physics for that I am thankful. I would like to thank 3SUN Enel Green Power in the persons of Cosimo Gerardi, Marina Foti, Carmelo Connelli and Fabrizio Bizzarri for the technological support and lab facilities. Finally, I want to thank my family for all their love and support over the years. I truly could not be where I am today without them.

Contents

List of Figures

List of Tables

List of Abbreviations

Al-BFS	**A**l **B**ack **S**urface **F**ield
AM	**A**ir **M**ass
BG	**B**ifacial **G**ain
BM	**B**ifacial **M**odule
BPV	**B**ifacial **P**hoto **V**oltaic
CA	**C**hrono **A**mperometry
CV	**C**yclic **V**oltammetry
CSW	**C**entral **S**pectrum **W**avelength
DFT	**D**ensity **F**unctional **T**heory
EASA	**E**lectrochemical **A**ctive **S**urface **A**rea
EC	**E**lectrochemical **C**ell
EVA	**E**thylen **V**inil **A**cetate
EQE	**E**xternal **Q**uantum **E**fficiency
e-NRR	**e**lectrochemical **N**itrogen **R**eduction **R**eaction
GHG	**G**reen **H**ouse **G**as
HER	**H**ydrogen **E**volution **R**eaction
HIT	**H**etero-junction (with) **I**ntrinsic **T**hin (layer)
IR	**I**nfrared **R**adiation
LSV	**L**inear **S**weep **V**oltammetry
MM	**M**onofacial **M**odule
MPP	**M**aximum **P**ower **P**oint
MPV	**M**onofacial **P**hoto **V**oltaic
NOCT	**N**ominal **O**perative **C**ell **T**emperature
NRR	**N**itrogen **R**eduction **R**eaction
NP	**N**ano **P**articles
OER	**O**xygen **E**volution **R**eaction
OVs	**O**xygen **V**acancies
PEM	**P**roton **E**xchange **M**embrane
PERC	**P**assivated **E**mitter (and) **R**ear **C**ontact
PCCE	**P**ower **C**onverction **C**ell **E**fficiecny
PV	**P**hoto **V**oltaic

RHE	**R**eversible **H**ydrogen **E**lectrode
SAC	**S**ingol **A**atom **C**atalyst
SCE	**S**aturated **C**alomelan **E**lectrode
SCR	**S**pace **C**harge **E**region
SHJ	**S**ilicon **H**etero **J**unction
Single	**A**tom **C**atalysts
SQ	**S**hockley **Q**ueisser
SR	**S**pectral **R**esponsivity
STC	**S**tandard **T**emperature **C**ondiction
STH	**S**olar **T**o **H**ydrogen (efficiency)
TCO	**T**ransparent **C**onductive **O**xide
TM	**T**ransition **M**etal
TOPCon	**T**unnel **O**xide **P**assivated **Con**tact
WPS	**W**hite **P**lastic **S**heet
WSF	**W**hat (it) **S**tands **F**or

Physical Constants

Speed of Light	c	$2.99 \cdot 10^8$	ms^{-1}
Boltzman constant	k	$1.38 \cdot 10^{-23}$	$m^2kgs^{-2}K^{-1}$
Neper number	e	2.73	#
Elementary charge	q	$1.6e-19$	C
Plank constant	h	$6.63 \cdot 10^{-34}$	m^2kgs^{-1}
Faraday constant	F	96485.33	$Cmol^{-1}$
Ideal gas constant	R	8.32	$JK^{-1}mol^{-1}$

List of Symbols

a	Distance	$[m]$
A	Device area	$[m^2]$
A_{el}	Electrode area	$[m^2]$
A_s	Ground element	$[m^2]$
BG	Bifacial Gain	$[\%]$
C	Bulk concentration	$[molcm^{-3}]$
C_0	Initial concentration of electroactive species	$[molcm^{-3}]$
D	Sun-Earth distance	$[m]$
$f(E)$	Fermi distribution	[#]
E_0	Standard electrochemical potential	$[V]$
E_c	Conduction band energy	$[eV]$
E_g	Energy gap	$[eV]$
E_v	Valance band energy	$[eV]$
E_F	Fermi energy level	$[eV]$
E_{back}	Solar radiation intensity on the module's back	$[Wm^{-2}]$
E_{front}	Solar radiation intensity on the module's front	$[Wm^{-2}]$
E_{fc}	Fermi energy level of electrons	$[eV]$
E_{fv}	Fermi energy level of holes	$[eV]$
E_p	Peak potential	$[V]$
$E_{p/2}$	Half peak potential	$[V]$
EY_{bif}	Bifacial energy yield	$[Wh]$
EY_{mono}	Monofacial energy yield	$[Wh]$
H_0	Sun luminosity	$[Wm^{-2}]$
I	Circuit current	$[A]$
I_0	Dark saturation current	$[A]$
i_C	Capacitive current	$[A]$
ip	Current peak	$[A]$
I_{mpp}	Current at maximum power point	$[A]$
I_{sc}	Short circuit current	$[A]$
i_f	Ideality factor	[#]

N_c	Effective density of state in conduction band	$[cm^{-3}]$
N_v	Effective density of state in valance band	$[cm^{-3}]$
Ng_0	Non radiative electrons generation	$[\#electrons \cdot s^{-1}]$
Nr_V	Non radiative photon flux	$[\#photons \cdot s^{-1}]$
n_0	Density of free electron in conduction band	$[cm^{-3}]$
n	Out of equilibrium density of free electrons	$[cm^{-3}]$
n_i	Intrinsic electron density	$[cm^{-3}]$
P	Power	$[W]$
p_0	Density of free holes in valance band	$[cm^{-3}]$
p	Out of equilibrium density of free holes	$[cm^{-3}]$
P_s	Electron-hole pair generation probability	[#]
P_c	Photon generation probability	[#]
P_{mppp}	Power at maximum power point	$[W]$
Q_{sun}	Solar photon flux	$[\#photons \cdot s^{-1}]$
Q_{cell}^{rec}	Cell photon flux	$[\#photons \cdot s^{-1}]$
Q_{cell}^{gen}	Cell electrons flux	$[\#electrons \cdot s^{-1}]$
Rr_V	Radiative photon flux	$[\#photons \cdot s^{-1}]$
R_{sun}	Sun's radius	$[m]$
S_{nit}	Interface recombination velocities	$[cms^{-1}]$
Sr	Incident solar photon flux	$[m^{-2}s^{-1}]$
T_{amb}	Average ambient temperature	$[C]$
T_{eq}	Equilibrium temperature	$[K]$
T_{front}	Front module temperature	$[C]$
T_{back}	Back module temperature	$[C]$
T_{module}	Average module temperature	$[C]$
V	Voltage	$[V]$
V_{mpp}	Voltage at maximum power point	$[V]$
V_{oc}	Open circuit voltage	$[V]$
—	————————	–
α	Absorption coefficient	$[cm^{-1}]$
β	Albedo	[%]
Ω_S	Incident solar angle	$[sr]$
ν_g	Energy gap frequency	$[Hz]$
ν_{scan}	Potential scan rate	$[Vs^{-1}]$
ν	Emitted photon frequency	$[Hz]$

Dedicated To my family…

Chapter 1

Energy and its storage

1.1 Introduction

Over the past decade, electricity demand has increased along with significant concerns about the energy crisis, energy prices, climate change and pollution. Furthermore, the rapid population growth besides the increasing energy request from the manufacturing and transportation sector represents the most important challenges of the 21st century. Renewable energies play an important role to overcome the energy challenge.

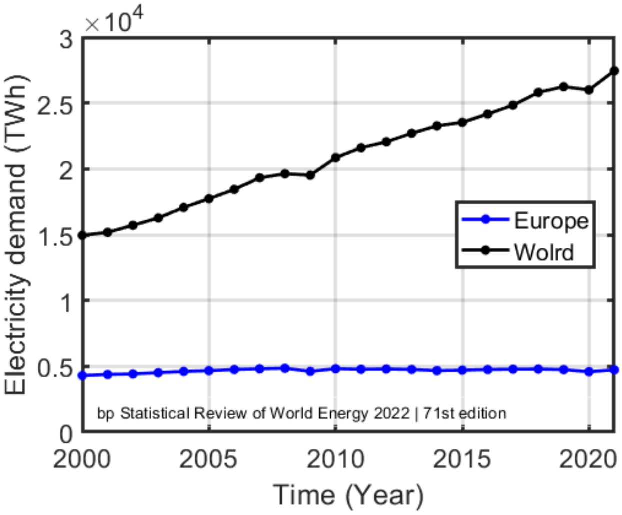

FIGURE 1.1: Global and European Electricity demand, normalized to electricity imports and exports.

Figure 1.1 shows the global demand for energy and its growth over a period of twenty years, reaching an increment of 50%. Unfortunately, fossil fuels remain the dominant part of energy sources and their use produces a huge amount of carbon dioxide emissions. Figure 1.2 shows that about 73% of the gases that cause the global greenhouse effect come from coal, oil, and natural gas combustion and use as fuel [1]. Meanwhile, toxic wastes are produced and dismissed into the environment during the manufacturing fossil fuel burning process. As a result, the dual issues of global climate change and lack of resources are challenging. Therefore, researching and developing new and sustainable energy sources is of primary importance as well as solving critical environmental issues.

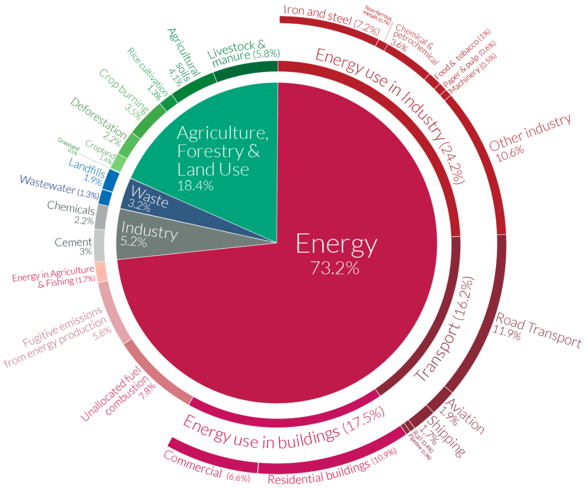

OurWorldinData.org – Research and data to make progress against the world's largest problems.
Source: Climate Watch, the World Resources Institute (2020). Licensed under CC-BY by the author Hannah Ritchie (2020).

FIGURE 1.2: Global greenhouse gas emissions by sector.[2]

1.2 Renewable resources

Twidell and Weir [3] defines renewable energy as:

"...energy obtained from natural and persistent flows of energy occurring in the immediate environment...".

An important aspect of renewable resources is that their flow through the environment is independent of whether energy is extracted, used or converted for use. As consequence,the flow of energy is not manufactured; it is simply exploited (or altered). Renewable energy is one pathway to a sustainable and green energy future. In this sense perhaps the most informative way of describing what renewable energy is to list some examples of the types of energy flows that are present in the immediate environment and can be tapped. These are wind energy, solar energy, wave energy, tidal current energy, biomass, hydro and geothermal energy.

FIGURE 1.3: Example of wind and solar plant.

1.2.1 Photovoltaic

With $1.7 \cdot 10^9$ TWh of energy per year, solar energy overwhelms the other forms of energy present on the earth. A small fraction of this impressive quantity of energy is sufficient to cover the actual energy demand that was estimated at $1.5 \cdot 10^5$ TWh. The conversion of this energy into electricity, via photovoltaic technology, is a powerful weapon to face the looming energy crisis exacerbates by the recent events in Europe. Presently, photovoltaics represents 3.6% of global energy production [4], but this figure is supposed to grow, in the best scenario case, to 10%.

In 2021 several efforts have been made to find a more efficient technology and the photovoltaic sector moved to crystalline cell production.

Currently, the more diffused cell design is that of the passivated emitter and rear contact (PERC) with almost 75% market share. New cell designs using technologies such as TOPCon, heterojunction and back contact with higher efficiency have caught the attention of the solar energy colossus that had converted their production lines and hit about 20% of the market in 2021 [5].

1.2.2 Bifacial photovoltaic

The bifacial photovoltaic system represents a promising technology for the future development of photovoltaics. Bifacial solar cells simultaneously collect incident solar radiation from the sun on the front side, such as conventional monofacial photovoltaic, and the albedo radiation from the ground on the back, plus some additional diffused light as is shown in figure 1.4. Therefore, compared with MPV, under suitable conditions, BPV can effectively increase the energy yield of PV modules and strings at reduced costs and according to the international technology roadmap for photovoltaics bifacial technology increase in the worldwide market share from 30% in 2020 to about 80% by 2031 [5]. Several bifacial photovoltaic technologies are available on the market but the most diffuse are: the passivated emitter rear contact cells (PERC), the tunnel oxide passivated contact cells (TOPcon), and the silicon heterojunction technology (SHJ) cells.

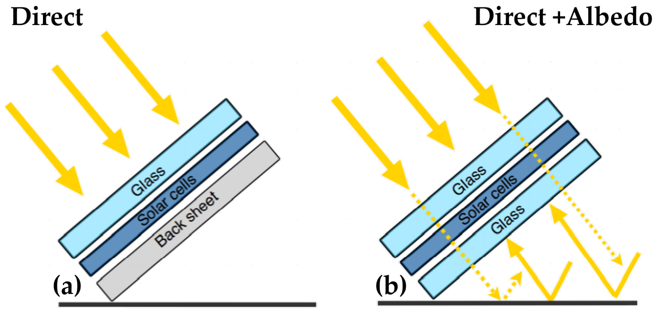

FIGURE 1.4: Monofacial (a) and bifacial (b) solar module[6].

Differences in cell structure result in different values of the bifaciality factor, defined as the ratio of the power at the maximum power point measured on the back divided by the front-side power at MPP under standard test conditions. Generally, the bifaciality factor ranges between 70% and 96% depending on the technology (PERC, TOPcon, SHJ)[7, 8]. Among the SHJ cells, the n-type ones are the most promising for bifacial photovoltaic, due to their high short-circuit current, open-circuit voltage, bifaciality, and for their low-temperature coefficient [9] compared with the most common p-type cells [10].

1.3 Energy storage

The process of storing energy that can then be used when needed or rather to perform a useful operation when direct energy production lacks, is called energy storage. Generally, in a world that looks to electrifying everything, the term energy storage is used to describe the process of converts the electrical energy, or correlated with electricity, in different forms that able to returning it to the grid when is requested. Therefore an energy storage can be achieved thanks to a device which can take or withhold energy from an energy network (in times of surplus), and return it to the network at a later time (of high demand).

Despite fossil fuels represent from various points of view as excellent energy carriers, their use contributes to the production of greenhouse gases including CO_2. The GHGs quantities produced are considerable and able to alter Earth's climatic system. As a matter of fact, plants and other organisms are not able to keep anthropogenic activities and as a consequence, GHGs produce detrimental effects on the living conditions of our planet.

A fascinating approach to overcoming the use of fossil fuels is to produce chemicals from renewable energy that can be enforced without replanning the established infrastructures. The key point is to employ H_2O and CO_2 as start feedstocks to be converted into green fuels in a shorter time compared with natural processes as depicted in figure 1.5.

Low-cost large-scale efficient energy storage would contribute to a platform on which to base a 100% renewable energy network. The intrinsic intermittent nature of renewable energy sources led to the necessity of a system that can store the excess energy and release it in case. Often, the energy peak demand does not coincide with the maximum renewable energy production. It is possible to define two ways to store

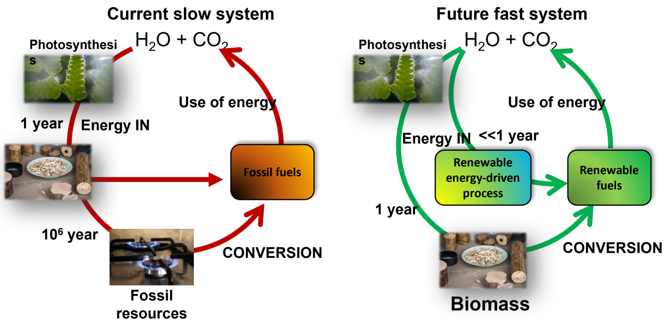

FIGURE 1.5: Conversion of H_2O and CO_2 via current and renewable energy driven process.

energy depending on the energy transformation. One case is where energy is transformed into another form, i.e. electricity into potential energy by gravity storage, and then reconverted into electricity and the second is where the energy is converted into energy vectors ,i.e. chemicals, or is used for charging electric vehicles, in this case, the electricity does not come back to the system.

1.3.1 Solar fuels

As suggested by the word fuel, solar fuels are all those chemicals or substances, in any material state, that can release chemical energy via chemical reactions, especially across a red-ox reaction with an oxidant agent like oxygen. Red-ox reactions can take place as combustion for heat production or in an electrochemical reactor to convert chemical energy into electricity, for example, using a fuel cell where hydrogen and oxygen react to form water and electrons can be extracted by electrodes. Fuel cells achieve high conversion efficiency than a burning system that needed other mechanical parts and works under thermal cycles. Solar fuels represent a sustainable way to store energy produced by renewable energy. A great example of solar fuel production and storage is provided by photosynthesis where light comes from the sun and is converted into harmless sugar or other carbohydrates by plants. However, this process remains under-performing if compared to the actual fossil fuel extraction. Presently, the most pledged solar fuel is hydrogen gas. Its free enthalpy of 141.5 $MJ \cdot Kg^{-1}$ is higher than the gasoline one equal

TABLE 1.1: Energy storage providing system.

Electricity-to-energy-to-electricity	Electricity-to-energy
Gravity storage	Hydrogen from Electrolysis
Batteries	Ammonia electrosynthesis
Pumped hydro storage	smart charging of electric vehicles

to 45.7 $MJ \cdot Kg^{-1}$. Furthermore, hydrogen combustion produces heat and water as by-products. Ultimately, hydrogen shows high versatility because it is a precursor of many chemicals.

1.3.2 Hydrogen production and uses

Hydrogen is the most abundant element in the universe and at the same time the most fleeting one on the earth [11]. Its high energy storage potential [12] makes it an ideal portable fuel to be used in portable applications, like fuel for the fuel cell vehicles. Hydrogen production is typically classified by different color depending from the process used to form it. In table 1.2 are reported the three commonest process and their color classification.

Brown hydrogen is produced via gasification, a process that converts coal or carbon-rich materials into hydrogen and carbon dioxide, this last is released as a by-product into the atmosphere.

$$C_{(s)} + 2\,H_2O_{(g)} \rightleftharpoons CO_{2(g)} + 2\,H_{2(g)} \tag{C 1.1}$$

Steam reforming is the process used for the production of blue hydrogen. The process uses steam to separate hydrogen from natural gas. Steam reforming does produce greenhouse gases, but modern technology can capture them by storage technologies and then store those emissions.

$$CH_{4(g)} + 2\,H_2O_{(g)} \rightleftharpoons CO_{2(g)} + 4\,H_{2(g)} \tag{C 1.2}$$

Finally, green hydrogen is obtained avoiding GHG emissions. The most common way to produce green hydrogen is via water electrolysis. A device called an electrolyser breaks the oxygen-hydrogen bound

TABLE 1.2: Classification of Hydrogen production.

Classification	**Raw material**	**Process**
Brown	Carbon	Gasification
Blue	Natural Gas	Steam reforming
Green	Water	Electrolysis

through by the electricity. The most common way to produce hydrogen through electricity is the water electrolysis via a polymer electrolyte membrane electrolyzer. PEM electrolyzers presents high operational flexibility and can couple with an intermittent renewable electricity generators [13]. Commonly, the water source for the electrolysis is provided by seawater desalination after further treatment for the purification. The needed electricity for hydrogen manufacture system is furnished by different power sources like on/offshore wind, solar PV plant, the local grid, and/or by discharging the battery [14]. An overlook of these hydrogen production routes are depicted in figure 1.6. The main advantage is that the needed electrical power to power the electrolyser is provided by renewable sources and this results in net-zero hydrogen production.

$$2\,H_2O_{(l)} \rightleftharpoons H_{2(g)} + O_{2(g)} \tag{C 1.3}$$

Different car manufacturers produce hydrogen vehicles that employ compressed Hydrogen gas, obtained from water electrolysis, as fuel that reacts with Oxygen via a fuel cell to form water and electrical energy. The Hydrogen energy storage drawback is its difficulty in transport and storage, indeed, the typical tank pressure is around 700 bar [15].

1.3.3 Ammonia production and uses

In the early years of the 20th century, Carl Bosch and Fritz Haber developed a method to produce ammonia (NH_3) on an industrial scale. The process is based on the direct synthesis of NH_3 from Nitrogen and Hydrogen using Iron-based catalysts. Initially, the high temperature needed for the synthesis, about 1000°C, and the cost of the first adopted catalysts (Osmium and Uranium) made the process prohibitive. The work of Carl Bosch permits solving the high technical requirements and

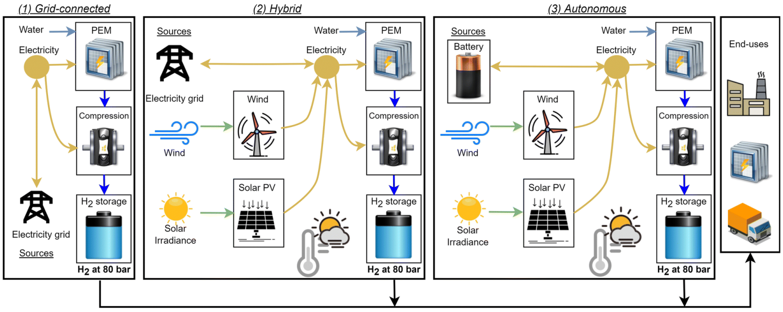

FIGURE 1.6: Simplified illustration of hydrogen production configurations: (1) grid-connected, (2) hybrid, and (3) autonomous, from left to right [14].

operating in more affordable conditions. The commercial production of ammonia began in 1913 with a temperature of 500°C and a pressure of 150 bar. For their discovery and development, Fritz Haber and Carl Bosch were awarded the Nobel Prize in chemistry in 1918 and 1931 respectively. A critical point in the Haber-Bosch process is ammonia decomposition which can occur above 500 °C [16]. NH_3 synthesis proceeds with a gas volume decreasing and, according to the Le Chatelier principle, high pressure has to be employed to improve the rate of reaction in favour of the products. The current industrial process parameters are the result of a compromise between the activity of the catalyst, the thermal stability of NH_3 and the reaction rate. Actually, the ammonia is synthesized by a continuous flow of Nitrogen and Hydrogen over a Fe-based catalyst supported on porous K_2O, CaO and Al_2O_3 substrates. This is only the main core of the entire process that is describe in figure 1.7 Thermodynamically, the reaction is exothermic and as consequence, the ammonia production is inversely related to the temperature.

$$N_{2(g)} + 3\,H_{2(g)} \rightleftharpoons 2\,NH_{3(g)}\ \Delta RH = -92\,Kjmol^{-1} \tag{C 1.4}$$

Nowadays, the Haber-Bosch process produces 230 million tonnes of anhydrous NH_3 per year, about the 96% of global production, with an efficiency of around 15% but the high pressure and continuous removal of ammonia increase the conversion efficiency up to 97% [17]. However, this industrial process also produces a ginormous amount of carbon dioxide, which is estimated to be 1-2% of the global CO2 produced

[18]. Indeed, the Hydrogen gas needed for the process is obtained by steam reforming of methane or natural gas at a high temperature (800 °C) a process that converts the CH_4 in CO and H_2. The CO at these temperatures is converted into CO_2. The estimated energy consumption for ammonia synthesis through the modern Haber-Bosch process is around 11 MWh/tNH_3.

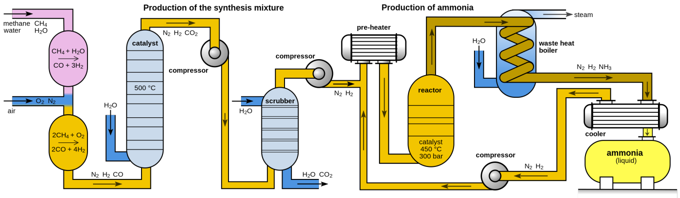

FIGURE 1.7: Diagram of the set-up of a Haber–Bosch plant. *CC BY-SA 3.0.*

In conclusion, the described Haber-Bosch shows many drawbacks, such as high CO_2 gas emission and consequentially environmental pollution, the enormous amount of energy consumption and the thermodynamic limitation of the reaction itself. A green alternative route for the NH_3 synthesis process is required to fight global warming and environmental pollution. Electrochemical ammonia generation through atmospheric nitrogen and a low temperature combined with the use of renewable energy can achieve the goal of low to zero carbon emissions.

In this regard, ammonia production is classified by the origin of the reactants, in particular hydrogen. The convectional categories, identified by the same color of the Hydrogen classification, are: brown, blue, and green.

1.3.4 Fuel cells

A Fuel cell is a device capable of generating electricity and heat through electrochemical reactions, basically, it is possible to see these reactions as the reverse of electrolysis. Indeed, the reactants are Hydrogen and Oxygen in gas form that react to form water and electrons that can be extracted and used suited applications [19]. The electrochemical reaction is reported below:

$$2\,H_2(g) + O_2(g) \longrightarrow 2\,H_2O + \text{Energy} \tag{C 1.5}$$

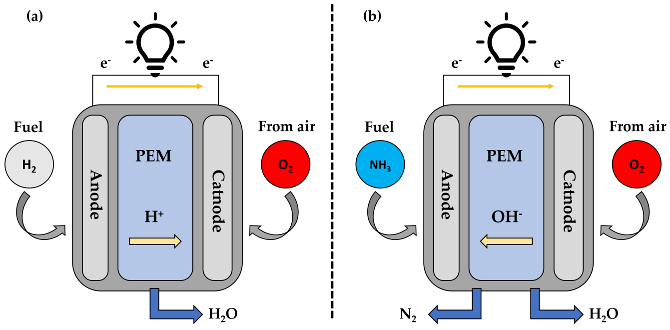

FIGURE 1.8: Operating principle of fuel cell (a) and direct ammonia fuel cell (b).

Figure 1.8 depicts the general principle of work of a fuel cell, where the hydrogen and oxygen gas passes through the anode and cathode respectively to react. At the cathode, hydrogen molecules go under oxidation and the formed electrons move in the circuit. Meanwhile, hydrogen ions across the membrane to reach the anode where the oxygen molecules are reduced in water. The generated electrons move from the cathode to the anode through the external circuit producing electrical energy.

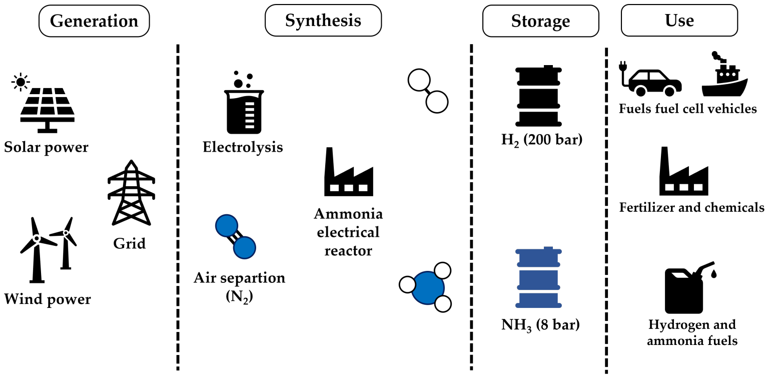

FIGURE 1.9: Renewable synthesis and use of green fuels.

TABLE 1.3: Comparison of heat engine and fuel cell [21].

#	Reciprocating diesel engine	Fuel cell
Capacity range	500 kW to 5 MW	200 kW to 2 MW
Efficiency	35% max	40-85 %

Fuel cells show a higher conversion efficiency compared to heat engines that use chemical energy and various mechanical part for the conversion of this energy into electricity, table 1.3 report a comparison between diesel engine and generic fuel cell. As a matter of fact, fuel cells convert directly chemical energy into electricity via the aforementioned method.

Ammonia can be similarly used as fuel. Indeed, the hydrogen that is contained in the ammonia molecule is accessible for the reduction of oxygen and then for electricity generation. In this case, the overall reaction is the follow:

$$NH_3 + O_2 \longrightarrow H_2O + N_2 + \text{Energy} \tag{C 1.6}$$

It's clear how important it is to produce green hydrogen and/or hydrogen carriers as ammonia for a zero carbon-footprint future. Figure 1.9 shows a possible sustainable scenario from the production of green energy to the use of green fuels. In the case of ammonia production more efforts must be made to permit ammonia fuel cells to be a truly sustainable source of energy [20].

1.4 Thesis outlook

This thesis presents research on the field of photovoltaic and the use solar renewable energy as reasonable source for green hydrogen production and investigates the possibility to produce green ammonia from Nitrogen gas. This research is dived in three section: (I) mathematical modeling of bifacial silicon solar modules electrical parameters under outdoor real conditions, (II) experimental evaluation of the influence of temperature and solar spectrum irradiance on the electrical performance of bifacial silicon solar cells, and (III) the coupling of photovoltaic technology with an PEM electrolyzer for the green hydrogen production and the research on a proficient catalyst for the electroreduction of Nitrogen to ammonia. After this introduction part there are 6 chapters that will describe below. The last chapter (7) provides overall conclusions of this thesis and lays out important avenues for future work.

The focus of Chapter 2 is theoretical fundamentals useful for understanding and recall some important physical and chemical aspect of the process described in this thesis.

Chapter 3, describe the mathematical model used for the optimization and evaluation of electrical performance of solar module taking in to account geometrical and thermal effects that can influence the energy yield and the efficiency this type of system. In particular, the type of grounds, and therefore their reflectance, beside the perimeter effect strongly influence the power output of bifacial solar cell and the modules. The model taking into account the spectral variation along the day and permit to estimate the annual energy yield in compare different module array installation, e.g. landascape vs. portrait. Furthermore, this model use a original 'equation' to estimate the thermal behavior of bifacial modules using the ratio between front and back generated photocurrent. The model was assessed by experimental outdoor measurements confirmed a delightful adherence to the modeled data.

Chapter 4 is focused on the effects of solar radiation, its spectral composition and temperature on the principal electric parameters, e.g. V_{oc} and I_{sc}. Attractive results have been obtained, especially the correlation between the redshift of the solar spectrum over the day and the current produced by bifacial photovoltaics. Besides, other correlations have been found and the results point out how bifaciality is a convincing technology.

Chapter 5 describes the optimization, evaluation and assessment of a photovoltaic-electrolyzer system that operated in outdoor conditions for several hours. This system consists in a three bifacial cells mini-modules electrical, with a total area of $730cm^2$ coupled with a proton exchange membrane electolyzer. The setup was optimized through modeling in terms of the number of cells, module height and inclination thank the model previously describe in chapter 3. Also, a comparison between the standard monofacial configuration and the bifacial one has been performed. Both the system is able to produce hydrogen with an high solar-to-hydrogen efficiency but, since the bifacial mini-module collect the albedo radiation from the ground, by the bifacial PV system achieved the best performance. The system exhibiting very good endurance, with no appreciable change in production and efficiency. The activities reported in detail in this chapter are a part of the Pecsys project funded by the European Commission under the Horizon 2020 programme. The goal of the project was to demonstrate a system for the solar driven electrochemical hydrogen generation with an area > $10m^2$.

Finally, chapter 6 explains the effort made for the optimization of iron base catalysts capable of dissociating the N_2 triple bond and to compete with the more favorable hydrogen evolution reaction. The catalyst consists in a mix of Fe_2O_3/Fe_3O_4 nanoparticles deposited on carbon cloth started from a solution containing $FeCl_3$. The implementation of an electrochemical activation procedure and the optimization of the morphology of the particle permits to produce ammonia under ambient condition.This encouraging results has been attributed to the sufficient exposure of edge sites, coupled to a larger proportion of $Fe_2{}^+/Fe_3{}^+$ and oxygen vacancies. This activity was a part of the TELEGRAM project ("Toward Efficient eLEctrochemical GReen AMmonia cycle"). The partners under the coordination of the **CNR-IMM** are the **Forschungszentrum Juelich**, the Competence Centre Thin Film and Nanotechnology for Photovoltaics Berlin (**PVcomB**) at the Helmholtz-Zentrum Berlin für Materialien und Energie GmbH (**HZB**) and the **Uppsala University**. The project aims is to demonstrate, at the laboratory scale level, a complete green ammonia carbon-neutral energy cycle, based on electrochemical processes, enabling the use of ammonia as a green fuel.

Chapter 2

Theoretical fundamentals

2.1 Photovoltaic

A solar cell is a device capable to converts the absorbed solar radiation energy into electricity thanks to the generation of electron-hole pairs. At the thermal equilibrium, an intrinsic semiconductor, that isn't subjected to photon flux, the electrons in the band states are distributed according to the Fermi distribution:

$$f(E) = \frac{1}{1 + e^{\left(\frac{E - E_F}{k \cdot T}\right)}} \tag{2.1}$$

where E_F is the Fermi level, at 0 K it is equal to Fermi energy.
This energy level and its position between the valence and conductive bands it's strongly dependent on the semiconductor material. In addition, the doping process alters considerably the Fermi level location. The doping process inserts atoms capable to donate (donors) or accept (acceptors) electrons into the crystal structure of intrinsic semiconductors that became extrinsic. The extrinsic semiconductor that has donors is called n-type and p-type when acceptors are present. In the same condition, the holes distribution follows the complementary distribution *1-f_e(E)*, where E_F is the same Fermi level deemed for electrons. At this point is possible to introduce the density of free electrons in the conduction band that is:

$$n_0 = N_c e^{\left(\frac{E_F - E_c}{k \cdot T}\right)} \tag{2.2}$$

where N_c is the effective density of state in the conduction band and E_c is the conduction band energy level. On the other hand, the density of free holes in the valence band is:

$$p_0 = N_v e^{(\frac{E_v - E_F}{k \cdot T})} \tag{2.3}$$

where N_v is the effective density of state in the valence band and E_v is the valence band energy level.

Combining the equations 2.2 and 2.3 an significant relationship can be found:

$$n_0 p_0 = n_i^2 = N_c N_v e^{(\frac{E_g}{k \cdot T})} \tag{2.4}$$

where E_g is the band gap and n_i^2 is the intrinsic electron density. Noteworthy is the independence of the product of the equilibrium electrons and hole concentration from the location of E_F.

When photons from the sun with energy higher than E_g impinging on the material, several electrons are promoted from the valence band to the conduction band, leaving in the former an electron vacancy, that is the holes.

The mean energies of these photo-generated electrons and holes reach rapidly the thermal equilibrium with the crystal structure because of the multiple collisions with the crystal lattice. Thereby, is possible to use the Fermi distributions at T_{eq} to evaluate the electrons and holes density. Under irradiation, both n and p are greater than the relative values in the dark n_0 and p_0, thus:

$$n \cdot p > n_0 \cdot p_0 = n_i^2 \tag{2.5}$$

In this situation, the Fermi energy of electrons, E_{fc} should be closer to the conduction band, whereas, the Fermi energy of holes E_{fv} should stay closer to the valence band [22]. Consequently, electrons and holes occupations in the bands now follows two separate Fermi distributions f_e(E) and f_h(E). As in Equations 2.2 and 2.3, the densities of electrons in the conduction band and in the valence band are, under illumination:

$$n = N_c e^{\left(\frac{E_{fc} - E_c}{k \cdot T}\right)} \tag{2.6}$$

$$p = N_v e^{\left(\frac{E_v - E_{fv}}{k \cdot T}\right)} \tag{2.7}$$

Similarly to equation 2.4 it is possible to obtain an important relation that come in useful in the next paragraph:

$$n \cdot p = N_c \cdot N_v \, e^{\left(\frac{E_v - E_c}{k \cdot T}\right)} \, e^{\left(\frac{E_{fc} - E_{fv}}{k \cdot T}\right)} \tag{2.8}$$

$$\frac{np}{n_i^2} = e^{\left(\frac{E_{fc} - E_{fv}}{k \cdot T}\right)} = e^{\left(\frac{qV}{k \cdot T}\right)} \tag{2.9}$$

2.1.1 Derivation of I-V characteristics

In the most simple case where exist only radiative pairs recombination and the all photons with energy higher then the band-gap produce an electron-hole pairs, it's possible to apply the SQ model to obtain the equations that are used in the rest of manuscript [23].

In figure 2.1 is reported the electrical scheme of a simple p-n junction solar cell surrounded by a black body both with a specific temperature. From the generalized Plank equation law for a black body at temperature T_s is possible to quantify the emitted photons.

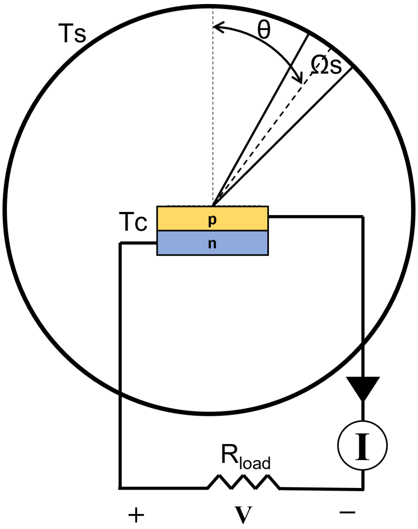

FIGURE 2.1: QS solar cell scheme.

In the case of maximal light trapping and incident solid angle Ω_S the equation is 2.10. Where P_s represent the probability that a photon generate an electron-hole pair, c is the speed of light in the vacuum, ν_g

is the frequency correlated to the energy-gap and ν is the frequency of the emitted photon.

$$Q_{sun} = A \cdot \frac{\Omega_S}{2\pi} \cdot \frac{P_s}{c^2} \int_{\nu_g}^{\infty} \frac{\nu^2}{e^{\left(\frac{h\nu}{kT_s}\right)} - 1} \, d\nu \qquad (2.10)$$

Similarly, the body of solar cell emits photons by raditive recombination according the following equation :

$$Q_{cell} = 2A \cdot \frac{2\pi \cdot P_c}{c^2} \int_{\nu_g}^{\infty} \frac{\nu^2}{e^{\left(\frac{h\nu}{kT_c}\right)} - 1} \, d\nu \qquad (2.11)$$

Where the term P_c is the probability that a e-h pair generate a photon and T_s is te temperature of the device. As stated before, in a ideal case where both the P_s and P_c are equal to 1, maximal light trapping and radiative recombination as only possible process of energy loss.

At the steady state condition the number of generated and recombined electron-hole pairs are the same. This is equivalent to write:

$$Q_{sun} - Q_{cell}^{rec} + \left[Q_{cell}^{gen} - Rr_{(V)} + Ng_{(0)} - Nr_{(V)}\right] - \frac{I}{q} = 0 \qquad (2.12)$$

where the superscripts *rec* and *gen* refer to raditive recombination from the cell as black body and spontaneous radiative generation respectively. The term Rr_V is the rate of radiative recombination, I is the current extracted from the device, $Ng_{(0)}$ and $Nr_{(V)}$ are the rate of non-radiative recombination and generation processes respectively. Recombination events is to consider proportional to emission one. Taking into account the electrons and holes density product np respect to the thermal equilibrium value n_i^2 is possible to determine these rates:

$$Rr_{(V)} = Q_{cell}^{rec} \cdot e^{\left(\frac{qV}{kT}\right)} \qquad (2.13)$$

$$Nr_{(V)} = Ng_0 \cdot e^{\left(\frac{qV}{kT}\right)} \qquad (2.14)$$

in these equation V is the voltage at the p and n terminals of the solar cell. Combining the equations 2.12, 2.13 and 2.14 in the case of $Q_{sun} = Q_{cell}^{rec}$, that correspond to the case of a black body at the same temperature of the cell, the net current flowing in an external circuit is:

$$I = -I_0 \cdot \left[e^{\left(\frac{qV}{kT}\right)} - 1\right] \tag{2.15}$$

where:

$$I_0 = q[Q_{cell}^{gen} + Ng_0] \tag{2.16}$$

is defined as the reverse saturation current. The current-voltage relationship, depicted in figure 2.2, for the solar cell subjected to photon flux and connected to a load when $Q_{sun} \neq Q_{cell}$, is equal to:

$$I = I_{sc} - I_0 \cdot \left[e^{\left(\frac{qV}{kT}\right)} - 1\right] \tag{2.17}$$

where:

$$I_{sc} = q[Q_{sun} - Q_{cell}^{rec}] \tag{2.18}$$

A better way to express the short circuit current consist to relate absorption coefficient α to the incident solar photon flux $Sr(\nu)$ and the thickness x of solar cell as follows:

$$I_{sc} = A \cdot \frac{q}{h} \cdot \int_0^{\infty} Sr(\nu) \cdot \alpha_{(\nu)} \cdot e^{\left(-\alpha_{(\nu)} \cdot x\right)}\, d\nu \tag{2.19}$$

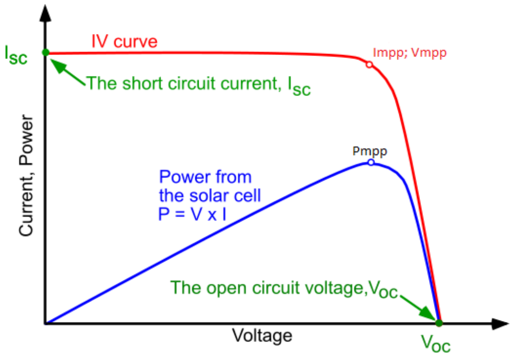

FIGURE 2.2: Current-voltage characteristic of a solar cell, adapted from pv-educational.

Under real condition the amount of photons that are converted in electron-hole pairs and then in electricity depends on the presence of defects and/or optical properties of the semiconductors [24]. At this point is useful to introduce the internal spectral response, SR(λ),that take into account the quantity of useful photons that contribute to the I_{sc}:

$$SR(\lambda) = \frac{I_{sc}(\lambda)}{qA(1-Sh)[1-R(\lambda)]Sr(\lambda)} \tag{2.20}$$

Where $(1 - Sh)$ and $[1 - R(\lambda)]$ are the portion of semiconductor shaded and the light reflected by the surface respectively. Therefore, the I_{sc} can be written as follows:

$$I_{sc} = qA(1-Sh) \cdot \int_0^\infty [1-R(\lambda)]Sr(\lambda)d\lambda \tag{2.21}$$

From equation 2.17 is possible to obtain another important relation. In particular solving the equation 2.17 for the case of $I = 0$ leads to:

$$V_{oc} = \frac{kt}{q}\, ln\left[\left(\frac{I_{sc}}{I_0}\right) + 1\right] \tag{2.22}$$

Where V_{oc} is the open-circuit voltage, that represents the electromotive force, which is the maximum potential difference when the total current pass through the circuit and the circuit is open.

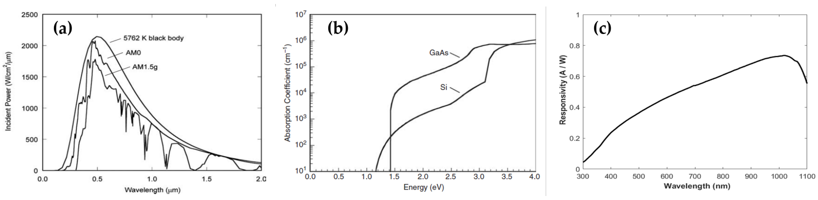

FIGURE 2.3: Standard solar spectra at different Air Mass values (a), optical absorption coefficient of silicon at 300 K(b) and silicon solar cell responsivity (c).

2.1.2 Solar radiation

As stated before, the sun's spectrum is commonly approximated to the 5800 K black body. Using this approximation the surface of the sun has a luminosity of $64 \cdot 10^6\ W/m^2$ (H_0). From this, it follows that the total emitted power is the product of the total surface of the sun by the power density. The Sun's surface is equal to $6.07 \cdot 10^{18} m^2$ so the total power output is $3.9 \cdot 10^{26} W$. This extraordinary amount of power can cover the whole energy demand of our society which is only 16 TW [24]. Due to the long distance between the earth and the sun, only a portion of the total sun radiance impinges on a body close to the earth's atmosphere. Indeed, the total solar radiance is now distributed over a greater surface. From an easy calculation using H_0 and the ratio between the radius of the sun (R_s) and the distance from sun-earth (D) the fraction of power density is 1370 W/m^2.

$$H_{earth} = \frac{R_{sun}^2}{D^2} \cdot H_0 \tag{2.23}$$

This radiation can be considered constant in the upper layer of the earth's atmosphere due to the low density of molecules and particles. The situation changes drastically near the surface of our planet. The atmosphere contains a lot of particles and molecules that scatter the light and absorb a considerable quantity of photons. Furthermore, the alteration of solar radiation depends on the location and the day of the year. Indeed, some local variations such as the level of humidity, pollution and clouds affect strongly the spectral content. Variations in the solar spectrum led to different responses by the solar cell. As discussed in previous paragraph the output current depends on the spectral composition of the solar radiation and the detector responsivity (or EQE). Besides, the scattering and reflection reduce the useful amount of solar radiation to convert into electricity by the solar cell. A well-known phenomenon correlated with scattering is the progressive redshift of light in the afternoon and morning. As matter of fact, the high energy photons are more effectively scattered and/or absorbed travel through a thick layer of atmosphere than the low energy photons (red). For this reason, in the morning and evening, the light from the sun appears much redder than in the middle of the day.

2.1.3 Air Mass

An important parameter that taking into account the path of the light through the atmosphere is the air mass (AM). The AM is obtained by normalizing the total path length to the shortest possible one that occur when the sun is directly overhead. From this quantity is possible quantify the reduction of the power intensity of the light passes through the atmosphere, which can be absorbed or scattered by air or particulate.

The Air Mass quantifies the reduction in the power of light as it passes through the atmosphere and is absorbed by air and dust. A simplified view of this phenomena is shown in figure 2.4.

A simple definition for air mass is:

$$AM = \frac{1}{cos\theta} \tag{2.24}$$

where θ is the zenith angle or the angle le from the vertical. It follows that when the sun is directly overhead, the air mass is 1.

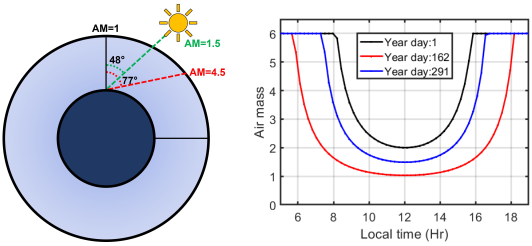

FIGURE 2.4: Graphical representation of different values of air mass (left) and variant of AM during the year.

The inherently fluctuation of the solar spectra and intensity of the impinging radiation during the day suggest to use a standard to facilitate the direct comparison between of solar cells electric characteristics to facilitate the direct comparison between measures obtained at different time and locations. At this regard, the standard solar spectrum called AM1.5G (where G refers to the global radiation), at Earth's surface, has a power intensity of 1000 W/m^2 and a light path length of AM equal to 1.5, that correspond to a zenith angle of 48°. The global radiation includes both the direct and diffuse radiation.

2.1.4 Albedo

The portion of the solar spectrum, or overall all electromagnetic radiations, reflected in all directions from a surface is called albedo. The reflection power of a surface is, of course, dependent on the wavelength of the electromagnetic radiation, the structure and composition of the surface and its angle of incidence with the surface. The albedo ranges from 0, total absorption, to 1 which is the case of total reflection. Figure 2.5

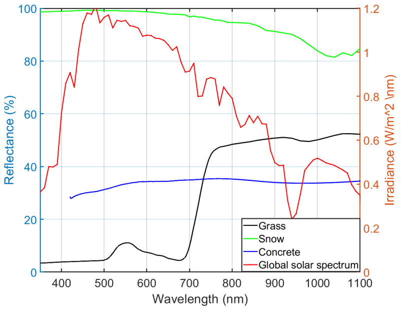

FIGURE 2.5: Reflectance of grass, snow and concrete; solar spectrum in the foreground.

shows the reflectivity of three ground surfaces compared to the global solar spectrum. White surface for instance snow reflects uniformly the entire visible solar spectrum, conversely, grass reflects wavelengths between 500 and 600 which are responsible for the green colour. Albedo plays a crucial role in the power output of bifacial solar cells which are capable to harvest light from the backside.

2.1.5 Silicon Heterojunction solar cell

The first concept of a heterojunction solar cell, with an intrinsic thin layer of amorphous silicon, was introduced by the former company SANYO which called this cell technology HIT (Hetero-junction with Intrinsic Thin-layer)[25]. Actually, SANYO is part of the company Panasonic and these types of cells are known as SHJ due to Panasonic's patent for the name HIT. The structure of the SHJ solar cell is shown in 2.6. The central part of the cell is composed of crystalline silicon, n or p doped, which works as a light absorber. This block states between two thin layers of intrinsic hydrogenated amorphous silicon (a-Si:H). The a-Si:H intrinsic layers are surrounded by n-type and p-type doped amorphous silicon layers that act as emitters. Finally, on the two doped layers, a film of transparent conducting oxide (TCO) is deposited to permit the current extraction from the cell assisted by screen-printed electrodes which are known as fingers and busbars. The TCO layers also work as an anti-reflection coating. The final result of SHJ solar cell is represented in figure 2.6 The SHJ technology has captured high-interest rates determined by the high power conversion efficiency and the possibility of reducing production costs. As a matter of fact, SHJ solar cells can be produced with a low thermal process below 200 °C and the symmetry of the cells reduces the complexity of the solar cell fabrication [26, 27]. Furthermore, the aforementioned symmetry of the front and the back of the solar cell made it suitable for the bifacial application. Some experiments show that bifacial SHJ solar cells perform better compared with monofacial conventional solar cells by 10% [28].

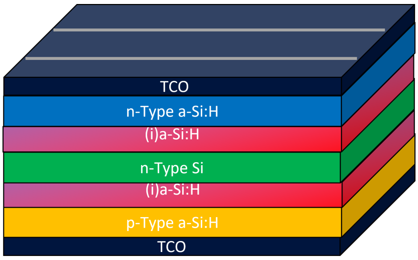

FIGURE 2.6: Silicon heterojunction solar cells with on n-type silicon (SHJn).

2.1.6 V_{OC} in SHJ cell

V_{OC} is strongly affected by the recombination processes at the heterointerface a-Si:H/c-Si and by the carrier transport in the solar cell. The V_{OC} for SHJ solar cells can be stated by the analytical model reported in [29]. In this manuscript the focus is on the case of low recombination in the c-Si layer and the main recombination path is at the heterointerface. In this case, the saturation current of SHJ cell is governed by the interface recombination velocity and electron concentration.

In this circumstance, is possible to write the following equation:

$$J_{0it} = qS_{nit}n_{it} = qS_{nit}N_c e^{\frac{-\Phi_B}{kT}} \tag{2.25}$$

Where Φ_B is the effective barrier height that is the sum of built-in voltage, define as the energy difference of the bulk Fermi level EF to the valence band EV, and S_{nit} is the recombination velocity of electrons at the interface. The band diagram of n-type a-Si:H/c-Si SHJ is depicted in figure 2.7.

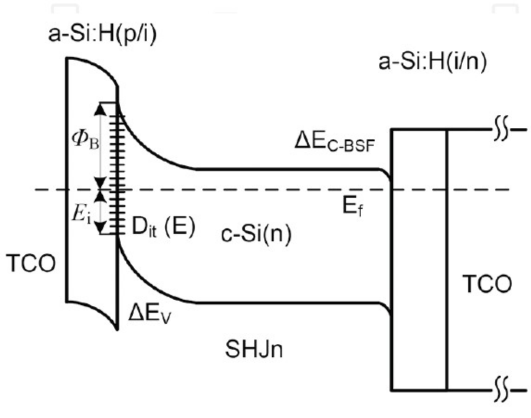

FIGURE 2.7: Band diagram of SHJn structure with sketched barrier for interface recombination ϕB at interface defects [29].

Recalling 2.22 and substituting J_{0it} it is possible to obtain the V_{OC} for the SHJ solar cell:

$$V_{oc} = \frac{\Phi_B}{q} - \frac{i_f kT}{q} ln\left(\frac{qN_V S_{nit}}{Jsc}\right) \tag{2.26}$$

Equation 2.26 indicates that V_{OC} depends on the illumination intensity, recombination properties at the heterointerface, recombination at the rear surface and in the c-Si substrate, and on the dopant activation energy of the c-Si substrate. The properties of the emitter seem to play no role in the V_{OC}. In fact, the parameters like doping, defect density and affinity (or band offset with c-Si) have no direct influence on the V_{OC}. However, all of these parameters affect the charge properties of the space charge region (SCR) of SHJ junction and thus carrier inversion at the heterointerface and consequently V_{OC}.

2.2 Electrochemistry

2.2.1 Electrochemical water splitting

Electrochemical water splitting and fuel cells are among the most promising energy technologies to address the future energy crisis and environmental pollution. The hydrogen evolution reaction (HER), a half reaction, occurs in electrochemical water splitting whereas the oxygen reduction reaction (ORR) half reaction, occurs in fuel cells. The most proficient catalysts are based on precious metal-based materials, such as Gold (Au), Platinum (Pt), Pt-group metals, and their alloys.

Specifically, water splitting, which stores energy in the form of hydrogen gas, has attracted much attention since the 1970's because it is a simple, environmentally friendly, two electron process [30]. Additionally, hydrogen is used in many industrial syntheses of fine chemicals as well as ammonium fabrication for agriculture [31]. Finding a clean method of generating hydrogen is thus of increased relevance.

Regardless of the device configuration, the overall water splitting reaction remains the same:

$$2\,H_2O \longrightarrow O_2 + 4\,e^- + 4\,H^+ \tag{C 2.1}$$

This reaction requires an energy input of ΔG = 237.1 kJ/mol at standard conditions, which corresponds to a thermodynamic voltage requirement of 1.23 V [32–34]. In a water splitting cell, the hydrogen evolution reaction (HER) takes place at the cathode and the oxygen evolution reaction (OER) takes place at the anode. These reactions are shown below as they occur in acidic electrolyte:

$$4\,H^+ + 4\,e^- \longrightarrow 2\,H_2 \tag{C 2.2}$$

The hydrogen evolution reaction is thought to involve three possible reaction steps:

TABLE 2.1: Hydrogen reduction reaction proposed mechanisms.

#	**Name**	**Reaction**
1	Volmer	$H^+ + e^- \longrightarrow H_{ad}$
2	Heyrowsky	$H^+ + H_{ad} \longrightarrow H_2$
3	Tafel	$2\,H_{ad} \longrightarrow H_2$

The HER can follow the Volmer–Heyrowsky or the Volmer–Tafel mechanism. Whether involved in the former or the latter mechanism the reaction requires that hydrogen atoms are adsorbed at the electrode surface, H_{ad}. The overall reaction rate is influenced by the free energy of hydrogen adsorption, ΔGH, as formerly described in the work of Parsons *et al.* [35]. The hydrogen-to-surface bond strength determines the rate. If the bond is too weak the absorption step may limit the whole reaction rate. Viceversa, if the bond is too strong the product desorption will be difficult and this limits the overall reaction rate. From these considerations, it is clear that the best option for optimal HER catalysts is to have a hydrogen adsorption energy as close as ΔGH = 0, that is the case where the hydrogen interacts neither too weekly nor too strongly [36, 37].

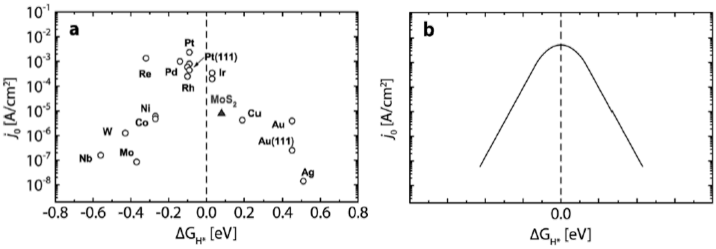

FIGURE 2.8: Exchange current density as a function of hydrogen adsorption free energy for various HER catalyst materials for (a) experimental and (b) theoretical values [38].

From the HER exchange current, which is a measure of the catalytic activity, is possible to plot the HER activity versus the ΔGH. What is obtained is a curve that remembers the shape of a volcano so-called "Volcano plot" reported in figure 2.8. The metal or materials on the top of the volcano presents the best HER activity, many of them are precious metal such as platinum, iridium or rhodium (see figure 2.8 a). Some materials are less efficient but are cheaper than noble metals like nickel alloys or other metal oxides.

2.2.2 Electrochemical Ammonia synthesis

The electrocatalytic N_2 reduction using water as the hydrogen source is regarded as a renewable approach under ambient conditions, offering a promising way for green and sustainable NH_3 production. Therefore, the development of a novel catalyst design is a crucial step for this challenge. In particular, many efforts are focused on the catalyst that can overcome the large energy barrier of N_2 reduction [39, 40]. Indeed, the high inertness of N_2 is the result of the strong triple bonding between two N atoms, that is 940.95 $kJmol^{-1}$. Furthermore, N≡N has an high ionization energy of 15.6 eV [41], negative electron affinity (-1.9 eV) and presents no polarity.

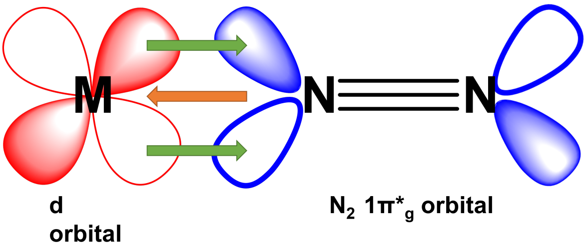

FIGURE 2.9: Schematic of the interaction between d-metal atom and absorbed N_2.

N_2 gas chemisorption on the catalyst surface, and consequent interaction with the active sites, weakens the triple bond by promoting hydrogenation [42]. The peculiar characteristics of the transition metal, belonging to the d-group, permit to promote activation of the N_2 triple bond thanks to the π-back-donation process depicted in figure 2.9. As a matter of fact, the metal of the d-group present unoccupied d-orbitals capable to receive the N_2 lone pair electrons, likewise, the occupied d-orbitals of the metal atoms are free to donate their electrons to the antibonding molecular orbital of the N_2 [43]. Despite this metal-nitrogen interaction being favorable for ammonia synthesis, because of the weakening of the nitrogen triple bond, transition metals can easily interact with hydrogen ions to form the metal-H bonds and at this point the HER compete with the NRR [44].

The NRR consists of multiple N_2 hydrogenation steps followed by electron transfer (figure 2.10). The main overall reaction of the NRR is:

$$N_2\,(g) + 6\,H^+ + 6\,e^- \rightleftharpoons 2\,NH_3\,(g) \qquad (C\,2.3)$$

For this reaction the reported E_0 is $-0.148 V vs. RHE$ which means that the overall energy to furnish at system is not prohibitive. Unfortunately, the bottleneck of this reaction is the first protonation which is an

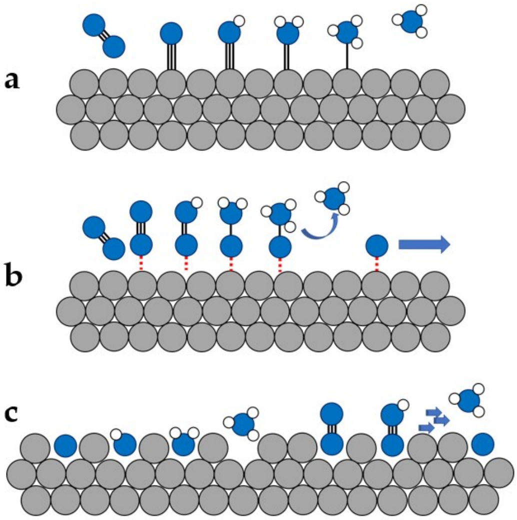

FIGURE 2.10: Schematic diagram of dissociative, associative pathway and Mars-van Krevelen hydrogenation mechanism.

endothermic process that involves a $\Delta H_0 = +37.6kJmol^{-1}$ and sets it as the rate-limiting step.

$$N_2 + H^+ + e^- \rightleftharpoons N_2H\ (g) \qquad (C\,2.4)$$

Although the first step is endothermic, even using an optimal catalyst, the other protonation reaction needed to form NH_3 is energy affordable. Proof of this lies in the overall Gibbs free energy that shows a negative value for the NRR [45], otherwise, the known nitrogen conversion processes by natural nitrogenase systems, the Haber–Bosch process, photocatalysis, and electrocatalysis would be impossible to perform.

2.2.3 Linear sweep voltammetry

In linear sweep voltammetry (LSV) a fixed potential (E) range is scanned from a lower limit to an upper limit. The potential influences the reaction rate and its change can be followed by acquiring the electric current (i) v.s the applied potential (V). From the slope of the time-V function is possible to obtain the voltage scan rate (v). The main factors that influenced the linear sweep voltammogram are the rate of the electron transfer reactions, the voltage scan rate and the chemical reactivity of the electroactive species. Usually, the voltammogram is obtained by plotting the current response vs the applied voltage and the scan begins in a region where the electron current is close to zero (non-faradaic current) then the potential is swept to more reductive or oxidant values and an electron current begins to flow. In these circumstances, a peak o more than one can appear in the voltammogram when the potential is close to the E_0, the current generally dropping after the peak due to depletion of the reactive species near the electrode surface if the solution is unstirred.

2.2.4 Cyclic voltammetry

As explained above, during the LSV the concentration of the reactant becomes ever closer to zero because of the lack of chemical species that can be reduced or oxidated. As a consequence, the current slowly drops and a large number of product molecules are located near the electrode. At this point, it is possible to reverse the potential scan, and then the oxidation or reduction reactions take place. The final result of the cyclovoltammetry (CV) experiment is the presence of an anodic or cathodic current peak quite similar to the former obtained in the first part of the voltage scan. CV is a robust method to analyse an electrochemical system and study the evolution of a reaction. The following equations are useful to derive important information about the system under study.

$$ip = (2.65 \cdot 10^5) \cdot A_{el} \cdot C \cdot \sqrt{D \cdot \nu_{scan}} \cdot \sqrt[3]{n_e^2} \tag{2.27}$$

where n_e is the number of transferred electrons, A_{el} is the surface area of electrode, D is the diffusion coefficient, C is the bulk concentration and ν_{scan} is the scan rate of the potential. Therefore, ν_{scan} could be derived by plotting ip versus $\sqrt{\nu_{scan}}$ when D and C are known.

Peak potential:

$$E_p = E_{1/2} - 1.109 \frac{RT}{n_e F} = E_{1/2} - \frac{28.5}{n_e} \tag{2.28}$$

Half-peak potential:

$$E_{p/2} = E_{1/2} + 1.109\frac{RT}{nF} = E_{1/2} + \frac{28.5}{n_e} \tag{2.29}$$

Nernstian wave follows:

$$\left|E_p - E_{p/2}\right| = 2.20\frac{RT}{nF} = \frac{56.6}{n_e} \tag{2.30}$$

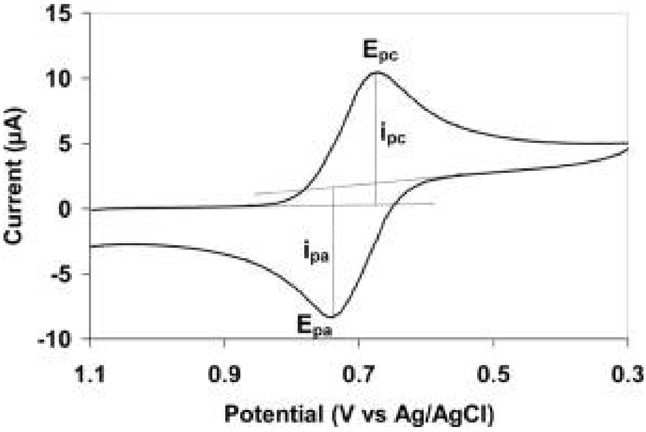

FIGURE 2.11: Example of cyclic voltammogram

The equations 2.28, 2.29 and 2.30 reflect that $E_{p/2}$ (potential at $ip/2$) is located in between E_p and $E_{p/2}$, and they are all independent from the scan rate. The last equation is also very useful to determine whether a given reaction is Nernstian or not.

2.2.5 Chronoamperometry

Chronoamperometry experiment consists of the recording of the faradic current at a fixed potential capable of oxidizing or reducing the analyte. A practical equation for describing the observed current, in the simple case of a planar electrode, is the Cottrell equation reported in 2.31.

$$i_t = \frac{n_e A_{el} F C_0 D_0^{1/2}}{\pi^{1/2} t^{-1/2}} \tag{2.31}$$

where C_0 is the initial concentration of electroactive species. At the very beginning of the experiment, the capacitive current, i_C contributes to the total current, however, it decays as a function of $1/t$ and commonly becomes minimal after a few *ms* or seconds.

$$Ne = \frac{\int_{t_0}^{t} i_t dt}{F} = \frac{Q}{F} \tag{2.32}$$

From the integration of the faradic current passes during the time of the experiment is possible to obtain the total charge and then the number of electrons, N_e, that take part in the reaction (see equation 2.32). This quantity is an important value for the estimation of the faradaic efficiency of an electrochemical reactor. Indeed from equation 2.33 it is possible to obtain the faradaic efficiency after the quantification of the electrochemical product (mol_p).

$$FE = \frac{mol_p \cdot n_e}{Ne} \tag{2.33}$$

Chapter 3

Effects of the Module Temperature on the Bifacial Photovoltaic Energy Yield

3.1 State of art

The prediction and calculation of the annual energy yield or the several electrical parameters of solar modules and arrays is an important topic in photovoltaics. Several mathematical and semi-empirical models have been proposed and described some focusing on bifacial modelling. In this section are reported a few of these. Yusufoglu et al. [46] proposed a model that can predict, through the calculation of the ground-reflected radiation and as consequence the part of radiation which reaches the rear side of the module, the annual energy yield based on reaching the rear side of the PV module. This model was refined by the implementation of the inhomogeneous radiation distribution that impinges on the back surface of the PV module [47]. Another critical aspect is the evaluation of the performances of bifacial photovoltaic solutions concerning the monofacial one. For this purpose, Shoukry et al. [48] develop a computational method that is useful for the evaluation of solar plant costs and the benefit of bifacial technology. Sun et al. [49] studied the optimisation of a stand-alone bifacial module for various geographic locations showing how a low power temperature coefficient is an important aspect in warm climate regions. From the lecture of the previous and other work, it's evident how the module temperature is a key aspect to consider since high temperatures have detrimental effects on the energy yield of many PV technologies. Therefore, before installing a solar plant a trustworthy prediction of the BPV energy yield based on the total striking solar radiation and the module temperature is needed to evaluate eventual power losses. One of the concerns about BPV modules is their temperature. Indeed, since they can collect solar radiation from both sides a portion of this energy of this power is transformed into a heat flux, and a higher module temperature is aspected. Nevertheless, the absorption of the impinging IR portion of the spectrum is reduced because of the absence of reflective surfaces like the aluminium screen in the Al-BSF monofacial cells. As consequence, the bifacial modules are more transparent in the IR and the temperature is maintained low compared to the abovementioned technology. This aspect of the module's thermal behaviour was analysed by Lamers et al. [50] which studied the impact of IR radiation on Al-BSF MPV modules. The study revealed that at low albedo, the MPV module shows a higher temperature compared with the BPV system. On the contrary, at high albedo conditions, the authors estimate that the BPV system becomes hotter than the monofacial one. Analogous results were described by Zhang et al. [51], who improve the previous model and also refined the studies by considering also the case of different ground materials and their reflectances. Other works report how the IR sub-bandgap absorption can influence the temperature of the PV module under bifacial operation. Patel et al.[9] referred that the IR sub-bandgap increasing BPV temperature. As stated above, these works stress the importance of using technologies with low power temperature coefficients, which is for example the case of SHJ solar cells. Previous works [50–52] took into account a direct comparison of performance and module temperature in bifacial and monofacial modes. However, in these studies, the differences in module temperature are severely influenced by the different solar cell technologies (PERC, PERT…) used in the modules. In summary, the problem of predicting the PV module temperature in BPV is a crucial aspect which needs further analysis and is treated in this chapter.

3.2 Experimental

The experiments were performed using two similar minimodules of 3 bifacial n-type SHJ. The SHJ cells were courteously offered by Enel Green Power which develops its technology at its 3SUN facility. Under

STC, these cells show a V_{OC} of 730 mV, an I_{SC} of 9.3 A, a BF of 90%, and a power conversion cell efficiency (PCCE) of 22.7%. The minimodules consisted of 3 cells connected in series via copper strips and laminated in a double transparent polyethylene shell with EVA backing. To avoid light collection from the rear side, one of the module's backside was covered with rigid white cardboard. In this way, the module operated as a monofacial module with a white back sheet. The white cardboard that was used had a low transmittance in the IR range. Some industrial white back sheets show transmittance can be quite large than the with card[53], and this led to a better thermal performance of the module. The site of the testes was settled in Catania, Italy (37°26′ N, 15° 4′ E). The data were collected from about 9 a.m. to 4 p.m. for 3 days in the period from 17 to 19 February 2021, on sunny days with no clouds. Figure 3.1 shows a picture of the minimodules under test. The modules presented a height of 55 cm, oriented facing south and tilted to the ground at 35 degrees. This installation setup was chosen to optimise front and backside solar radiation and ground albedo collection, according to our laboratory's previously developed model [54].

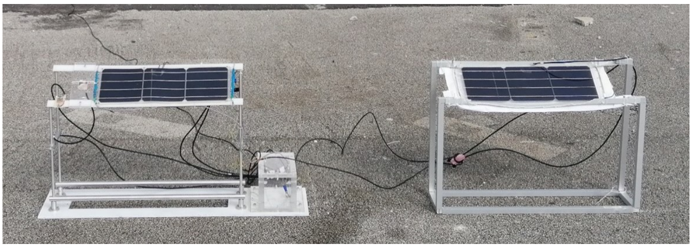

FIGURE 3.1: Image of the experimental setup: front view of the two minimodules, with the bifacial on the left and the monofacial on the right.

The minimodules were positioned on a portion of asphalt which presents an average normal incidence reflectivity of 30% over the 300–1100 nm range, as reported in Privitera et al. [55]. An MS-40 EKO pyranometer tilted at 35° was used to measure solar irradiation intensity hitting on the PV minimodules. similar to the minimodules. The minimodule temperatures were recorded employing two tiny thermoresistances placed in close thermal contact with the front and back of each minimodule. To prevent misinterpretation caused by radiant heating the probes were covered with reflective white cardboard about of 4 mm^2 to shield solar radiation. To optimize the yield bus bars were chosen as a perfect site for thermal analysis, thus producing negligible PV cell shadowing.

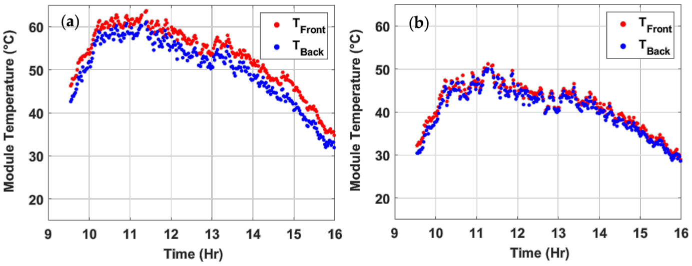

FIGURE 3.2: Example of measured temperatures of the minimodule on the front and back surfaces as a function of time for bifacial (a) and monofacial (b) minimodules measured in one of the days of measurement.

Figure 3.2 shows the obtained temperature from the thermoresistances. It is evident how T_{front} is larger than T_{back} in all cases. This can be explained by the different amounts of solar radiation that arrives on the front and back surfaces of the PV minimodules, an important clue is given by the large difference in short circuit current values measured in bifacial and monofacial systems at all times, as shown in the following section and reported in figure 3.5. The symmetric composition of the modules permits to assume that, with both sides laminated with the polymer and the same process, the module temperature (T_{module}) is with a negligible variation in the average of the temperatures measured on the front and the back. Then is possible to write:

$$T_{module} = \frac{T_{front} + T_{back}}{2} \tag{3.1}$$

Notwithstanding more complex models of modules, temperatures have been formulated in literature, implementing heat transmission throughout the module layer [56]; the minimodules under test present a polymer lamination of only 1 mm thick. For these reasons, equation 3.1 represents a reasonable assumption. The current–voltage (I–V) characteristic of each PV minimodule was obtained by a Kelvin probes method. The flowing current was measured by the voltage drop across a 20 $m\omega$ resistor connected in series to the load, in the present case a power MOSFET. The voltage across the module was, obtained by an STP60NF06 power MOS repeatedly driven from an OFF to an ON condition by a linear staircase signal at 0.2 Hz applied to the transistor gate. Data were continuously acquired through a USB6343 National Instrument data logger.

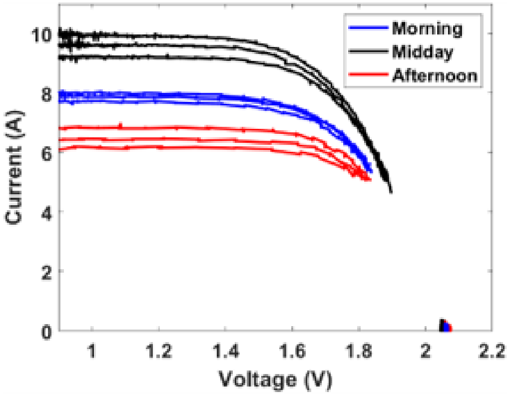

FIGURE 3.3: Experimental I–V curves collected from the bifacial minimodule in one of the days of measurements.

The data region between ≈ $1.8V$ and ≈ $2V$ the I–V data were filtered because affected by noise due to the acquisition system. These data points were eliminated and excluded from further data analysis since it does not add any further information. Anyway, it is important to observe that data filtering did not alter the capacity to extrapolate the values of the I_{SC}, V_{OC}, and Pmpp. These quantities were obtained from the experimental I–V curves reported, for example in figure 3.3. Each I–V curve was repeatedly taken on each 90 s, obtaining about 250 data sets on average during each day. With this setup, was possible to follow the daily evolution of the PV system characteristics with high time resolution and accuracy in the measurements of current and voltage of about 0.5% and 0.1%, respectively. Finally, the ambient temperature data were collected from an in-site weather station.

3.3 Results and Discussion

3.3.1 Module Temperature

Figure 3.4b reports the monofacial and bifacial minimodule temperature and the ambient temperature collected during one day and the averaged over the three days of testes. In the morning temperatures were low, reaching their maximum at midday when solar irradiance is at its zenith, and decrease moving to the afternoon. Due to the antireflection coating and the consequent dark colour, module temperatures were much higher than the air temperature since they absorbed solar irradiation and warmed up. As visible in figure 3.4b, the bifacial module is up to about 12 °C warmer than the monofacial module for all test days. Figure 3.4 reports also the module temperature profiles calculated according to the proposed model, better discussed further in the text, which resembles the experimental trends.

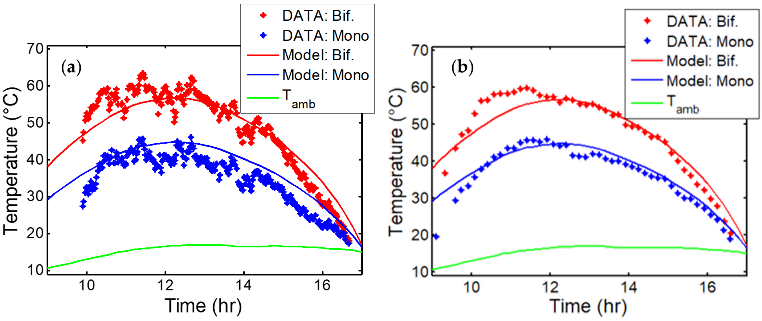

FIGURE 3.4: Data of a single day of module temperature compared with the values predicted by the model (a) and average values compared with the model (b). Ambient temperature is also reported as reference.

3.3.2 Module Electrical Parameters

Figures 3.5, 3.6 and 3.7 report, respectively, the experimental data of I_{SC}, V_{OC}, and electrical energy yield at the maximum power point as a function of time-averaged in the 3 days of measurements. To evaluate the energy yield the cumulative energy produced by each minimodule at its maximum power point was calculated since the start of the measuring period (about 9 a.m.). In the mentioned figure are present also the modelled curves of the experimental data. The green line at the bottom of figure 3.5 refers to the calculated I_{SCback} contribution to the bifacial PV module I_{SC} due to the albedo light harvest by the rear side of the PV cell. The I_{SC} difference between bifacial and monofacial operation is caused by the contribution of the current generated at the back of the

PV module. From the comparison between the monofacial module and bifacial I_{SC}, is possible to provide an estimation of the ratio of the solar radiation flux that arrives at the back surface (Abot) for the one collected by the front (Atop).

Two photodetectors oriented similarly to the PV minimodules were used to measure the ratio Abot/Atop. This system is similar to an albedometer, indeed, one of the cells faces up and the other faces down towards the ground (for clarity the figure is shown in the next chapter). The mean albedo is about 17–20%; which means that the radiation impinging on the back is about 17–20% of the radiation incident on the front. The electrical model depicts this feature nicely as it is possible to see in figure 3.5.

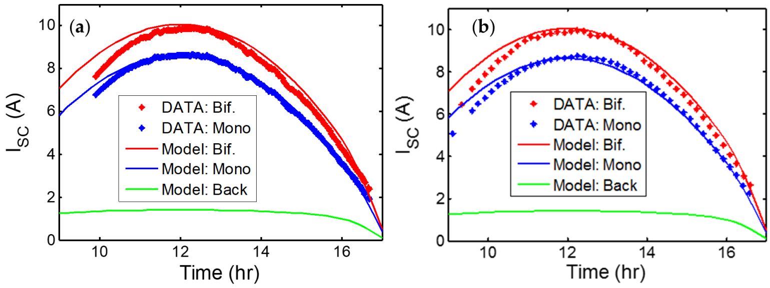

FIGURE 3.5: Data of a single day of module I_{SC} compared with the values predicted by the model (a) and average values compared with the model (b). The model allows also to separately calculate the current generated by the back of the module.

Thank to the thermal stability of the SHJ solar cells, the bifacial PV minimodule shows a higher current output compared to the monofacial one noticeable in the I_{SC} even if the V_{OC} is moderately lower to the higher temperature. However, the bifacial module presents a remarkably larger energy yield at the maximum power point.

Figures 3.4-3.6 also report the averaged experimental data and the calculated best-fit curves. The good agreement with the experimental data permits to performing of quantitative evaluations of the energy yield of bifacial PV systems. A similar approach was followed for the other quantities, and the model was confirmed against the average and single-day data.

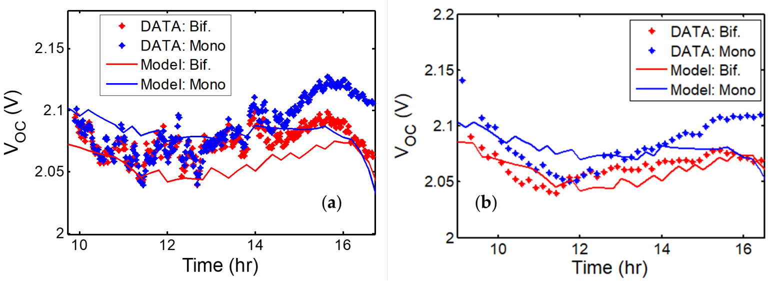

FIGURE 3.6: Data of a single day of module V_{OC} compared with the values predicted by the model (a) and average values compared with the model (b).

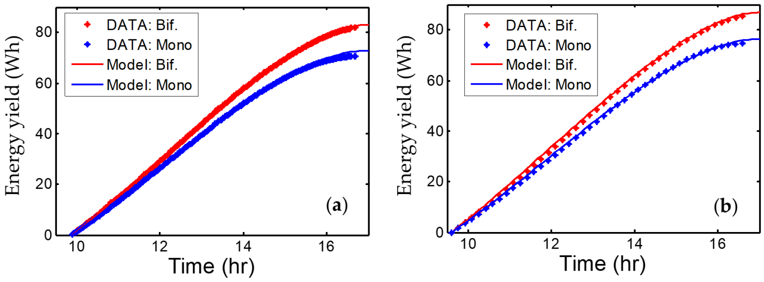

FIGURE 3.7: Data of a single day of module energy yield compared with the values predicted by the model (a) and average values compared with the model (b).

3.3.3 Model of Bifacial PV and Data Fitting

The proposed model is an update of a previous one reported in refs. [54, 57]. That model was proposed to evaluate the I–V characteristics and energy yield of PV bifacial modules and strings. The actual model assumes a complete three-dimensional (3D) geometry, that surpasses the simplification of a bidimensional (2D) approximation. In fact, while differences in backside irradiance, due to the position of the modules in the string, can be neglected for longer strings, in the case of a shorter string the irregularity of the ground led to important differences in terms of power output [58]. With this in mind, the model takes into account the impinging solar radiation divided into the direct, diffuse, and reflected components, modelled by using the ASHRAE model [59], the Global

Solar Atlas database [60], Liu and Jordan's isotropic model of diffused light [61], and the nominal operating cell temperature (NOCT) model [62]. The solar radiation impinging on the bifacial PV device was separated into two parts, that is, the I_{SC} component due to the solar radiation impinging on the front $I_{SCfront}$, and the I_{SC} component due to the albedo radiation diffused by the ground, I_{SCback}. $I_{SCfront}$ was calculated by equation 3.2 considering only the direct and the diffused radiation incident on the front, exactly in the same way as in the case of the monofacial solar cells. Vice versa, I_{SCback} was calculated by equation 3.3 only in the case of bifacial modules, and it was obtained by integrating over all the infinitesimal elements of the ground on which the PV system was installed. All the pieces of ground acted as isotropic light sources diffusing light proportionally to the global horizontal radiation and the ground albedo as shown in figure 3.8. However, the shaded regions were set as perfect absorbers to consider the effect of the shadowing on the performance of the bifacial solar module.

$$I_{SCfront} = A \cdot \int_{E_g}^{\infty} S_{front}(\lambda) \cdot EQE_{front}(\lambda)\, d\lambda \tag{3.2}$$

$$I_{SCback} = A \cdot \int_{A_s} d\Omega \cdot shadow\, dA_s \cdot \int_{E_g}^{\infty} S_{back}(\lambda) \cdot EQE_{back}(\lambda) \cdot \beta(\lambda)\, d\lambda \tag{3.3}$$

The $I_{SCfront}$ was calculated as the integral of the front side EQE with the spectrum of the solar radiation incident to the front. The I_{SCback} was obtained by integrating all the infinitesimals ground elements and considering them a centre of the diffused radiation, the intensity of this radiation is proportional to the solid angle between the ground element and the cell back. The model uses wavelength-resolved ground albedo, backside EQE, and the spectrum of the horizontal component of solar radiation. For the simulation of a larger module array, a significant ground area was considered to permit an evaluation of the perimetral effect due to module self-shadowing. Furthermore, the relation between module glass reflectance as a function of the incident angle was taken into account to correct for the increasing reflectivity which reduces the collected radiation.

The overall I_{SC} for the bifacial module was calculated as the sum of $I_{SCfront}$ and I_{SCback}, while the cell current–voltage characteristics were calculated according to simple current source/single diode lumped element circuit model reported in [63] considering the series of all the PV cells. For the minimodules, the computation simulate and numerically calculated the series of 3 cells. In the case of a large module modelling, the computation takes into account the series of 432 cells in a string of 6 PV modules. The V_{OC} was obtained as the PV string voltage when the current is equal to 0 A, whilst the PMPP was evaluated as the maximum of the power produced by the system.

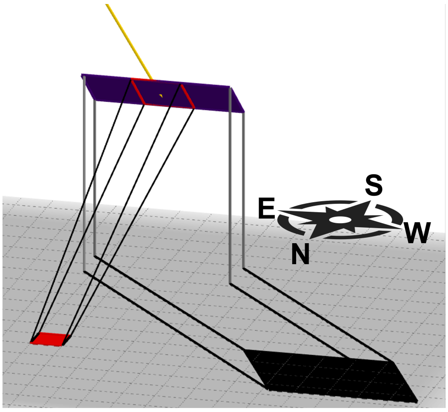

FIGURE 3.8: 3D representation of the simulated system.

One of the most important parameters for the PV cell circuit model is the cell temperature which, needs to be properly modelled. Different models use different approaches to model the module temperature [64]. For simplicity and to not burden the computational speed, the proposed model ignores the effect of wind. By the way, the outdoor measurements were performed under light breeze conditions [65] that correspond to the $1 ms^{-1}$ wind speed used for measuring the NOCT.

One of the most important parameters for the PV cell circuit model is the cell temperature which, needs to be properly modelled. Different models use different approaches to model the module temperature [64]. For simplicity and to not burden the computational speed, the proposed model ignores the effect of wind. By the way, the outdoor measurements were performed under light breeze conditions [65] that correspond to the $1 ms^{-1}$ wind speed used for measuring the NOCT. Furthermore, Zouine *et. al.* reported that models that include wind may be even less accurate than those that do not consider this factor, especially in non-windy locations [66] From these assumptions, NOCT model was used as a base to adapt for describing the experiment. Moreover, the NOCT parameter is usually used for commercial and industrial purposes, and for this reason, a correction that extended the model to BPV would be desirable. The experiments reported in this thesis experimentally measured the PV module temperatures both in bifacial and monofacial cases, and noticeable differences were observed, as shown in figures 3.4 and 3.2. Therefore, to take into consideration the large observed temperature difference, the model of refs.[54, 57] was refined as follows: The conventional equation for evaluating monofacial module temperature is:

$$T_{bm} = T_{amb} + E_{front} \cdot \left(\frac{NOCT_{bif} - 20}{800} \right) \tag{3.4}$$

where E_{front} is the intensity of the solar radiation impinging on the PV cell front, to be expressed in Wm^{-2}, while NOCTmono is the nominal operating condition temperature to be expressed in °C. The above equation 3.4 is suitable only for monofacial modules. When bifacial modules are modelled is needed to consider the radiation that hitting on the back, in contrast with monofacial modules, where the radiation impinging on the module's back surface is largely reflected away by the white back sheet. It follows that the temperature of the monofacial module is more stable than the bifacial one. Indeed, the ground radiation does not contribute to the module temperature. The large temperature differences observed experimentally between monofacial and bifacial modules can be explained by the irradiance mismatch (figures 3.4 and 3.2). Based on such premises, a modified equation similar to equation 3.4 is introduced as follows:

$$T_{bm} = T_{amb} + (E_{front} + E_{back}) \cdot \left(\frac{NOCT_{bif} - 20}{800} \right) \tag{3.5}$$

where T_{bm} is the temperature of the bifacial PV module, and $NOCT_{bif}$ is the NOCT of the bifacial PV module. Despite simply adding the radiation impinging on the back surface to E_{front}, it is more truthful to consider this additional term by concerning the real contribution to the heating processes. Indeed, calculating the ratio between I_{SCback} and $I_{SCfront}$, the amount of dispersed radiation is taken into account insofar

TABLE 3.1: Best-fit values of the proposed model compared with the STC cell values.

Parameter	Best-Fit Value	Measured STC Value
PV cell I_{SC}	9.15 A	9.30 A
PV cell V_{OC}	720 mV	730 mV
PV cell Rs	6 $m\Omega$	3 $m\Omega$
PCCE at mpp	21.1%	22.7%
αT	$-0.26\%°C^{-1}$	$-0.26\%°C^{-1}$
Mini-module NOCTmono	42 °C	-
Mini-module NOCTbif	47 °C	-

as only the absorbed radiation participates in the thermal motion. As matter of fact, as previously described, the main factor in the calculation of I_{SC} is the EQE, which is independently considered for each side of the bifacial cell. As a consequence, the portion of irradiance that is reflected or transmitted is excluded from the calculation and does not contribute to cell heating. Then, from these assumptions and using the model above described and refined implementing the equations 3.4 and 3.5, the best-fit curves of the model to the data of figures 3.2–3.7 were calculated.

The fit parameters used for the modelling are the NOCTbif, NOCTmono, the power temperature coefficient αT, I_{SC}, V_{OC} (at module STC), and the series resistance Rs. The obtained best-fit values are almost the average values reported in a work that used the same cell technology in the case of bare SHJ cells in STC [67]. The slight divergences in the order of 10% around the reported STC values were found for the V_{OC} and I_{SC} but are consistent with the lamination process. Rs parameter has shown an increase up to a factor 2 of the STC. This increment is expected due to the bar-bussing and lamination processes which can produce some ohmic losses and the consequent worsening of the series resistance. The best-fit values used for the curves calculated in figures 3.2–3.7 are reported in table 3.1.

The prototypal nature of the module structure and lamination process led to an anomalous best-fit value. These entries, indeed, correspond to lower performances if compared with the bare cell parameters measured in STC, which often happen in these cases [68]. Nonetheless, the founded best-fit values are close enough to the initial STC cell parameters, and the resulting curves calculated by the proposed model fine imitate the experimental data, in the case of PV system energy yield, and for the other fundamental physical parameters as module temperature, V_{OC}, I_{SC}).

Regarding the best-fit value of $NOCT_{bif}$, it is visible that the result is larger than $NOCT_{mono}$. This result was expected because the operative conditions to measure the NOCT, are limited to the case of monofacial module certification. Indeed, the module is irradiated at $800W/m^2$, at 45° inclination, and 20° ambient temperature, and with a wind flowing at 1 m/s. Given the definition and the previous assumption, it appears reasonable to assume that $NOCT_{bif}$ is larger than $NOCT_{mono}$ since, under solar irradiation in an open field, the bifacial module collects the albedo light from the ground. Therefore, more solar power is collected by the bifacial module and dodged by the monofacial module, resulting in a higher module temperature.

3.3.4 Model Extrapolations to Annual PV Energy Yield and Effect of αT

The evaluation of the model through the fitting of the experimental data permits the extrapolation of realistic parameters for a larger PV system. In particular, PV module strings of many modules rather than minimodules of a few cells were taken under test for the calculation of the yearly energy yields rather than daily yields. For this purpose, a realistic PV system configuration was chosen and considered a large ground area to minimize the perimetral effect that can affect the comparison between monofacial and bifacial PV strings[54]. Furthermore, the perimeter size was optimized to achieve the maximum possible gain of the BPV energy yield.

As for the minimodules, the latitude chosen for the comparison was the latitude of Catania (37°26′ N, 15°4′ E) and the same temperature profile (Catania in the year 2017, as reported in [25]). For the rest of the discussion, the systems analysed were assumed to be oriented facing the south and with a tilt of 35°, these parameters follow the experimental setup just described because this is the tilt angle that has shown the maximum annual energy yield. Figure 3.9 reports the relative bifacial gain, defined as:

$$BG = 100 \cdot \frac{EY_{bif} - EY_{mono}}{EY_{mono}} \tag{3.6}$$

where EY stands for energy yield, according to the temperature profile of Catania in 2017. The case considered were two: the first is a three-bifacial cell minimodule installed at an average height of 55 cm (the outdoor studied case depicted in figure 3.1 the latter is a string of 6 modules of 72 cells (6 cells high and 12 cells wide) of $1m * 2m$ arranged in a $2 * 3$ configurations (2 modules high and 3 modules wide), installed at an average height of 2 m (red curve). Both cases were in a landscape-type installation, i.e., with the PV system long side along the east-west direction.

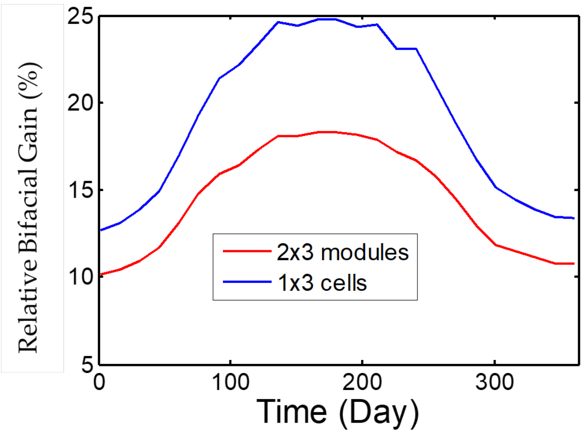

FIGURE 3.9: Modelled relative bifacial gain over the course of the year for a minimodule (blue) and a string of six modules (red).

Figure 3.9 shows clearly that the system with the largest energy yield is the three-cells module. The size of the PV system is quite larger than the mini-modules and this increased the self-shadowing effect. Indeed, the differences in the ground illumination and then in the reflected light that arrives at the rear of the PV cell become uneven. Since all cells are in series, the PV cell with the worst backside illumination drives the entire current and as consequence, the one with the lowest I_{SC}SC will dictate the energy yield. This effect becomes much stronger for a large string of 6 modules with 432 cells; therefore, the PV relative bifacial gain is clearly lower. However, the calculated relative bifacial gain remains always above 10%, with a clear and remarkable advantage of energy yield. These results are in good agreement with other experiments reported in refs. [69–71] and with the calculated values reported in refs. [72, 73]. Noteworthy is that, according to the model, the maximum difference in temperature between bifacial and monofacial modules is between 9 °C and 12 °C at the latitude of Catania throughout the year.

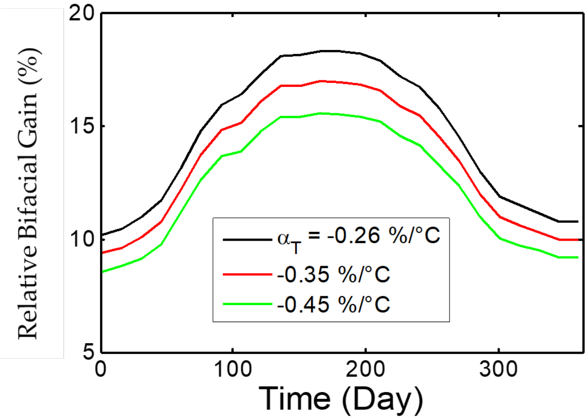

FIGURE 3.10: Modelled percent increase in relative bifacial gain over the course of the year of a six modules string for different values of the power temperature coefficient.

The relevance of the αT parameter for application in the bifacial setup was investigated. PV technologies with low αT (in absolute value) present an advantage, especially for application in warm climate regions. This feature is crucial in the case of bifacial systems that tend to become hotter than monofacial ones. Hence, one expects that the relative bifacial gain will be better in technologies with low αT in absolute value. To quantify the advantage, a calculation using the model here proposed was performed.

Figure 3.10 shows the relative bifacial gain calculated for a year considering the temperature profile of Catania in 2017 and for the case of one string of 6 modules in a 2 x 3 landscape configuration, as previously described. The parameters used as inputs for the model are the same as reported in Table 1 for the previous calculations, except for αT, which ranged from $-0.26\%/^\circ$ to $-0.45\%/^\circ$. These values correspond to the most diffuse thermal coefficients for silicon PV technologies currently on the market. As expected, as αT increases in absolute value the relative bifacial gain decreases. From the best to the worst case, the change is noticeable, of about -20%. In all cases, however, the bifacial systems show a strong advantage in terms of energy yield.

Chapter 4

Effects of solar spectrum and albedo on the performance of bifacial SHJ mini-modules

4.1 Experimental setup

The experimental setup employed for the experiment is quite similar to the one described in chapter 3. The cell electrical parameters and mini-modules installed are summarized in 4.1.

Moreover, the solar spectrum was monitored in clear-sky conditions using the system depicted in figure 4.1d. The system consists of a monochromator (Newport, model: CS130-RG-1-MC), an optical fibre mounted on a dual-axis tracker (which continuously tracks the sun position) and connected to the input of the monochromator to collect the incident solar light and a Si photodiode at the monochromator output. The system was used to measure the solar spectrum evolution from 350 nm to 1100 nm as a function of solar time. The ambient temperature data were collected from a nearby weather station.

The solar irradiation was measured by using an MS-40 EKO pyranometer. The pyranometer was tilted at 35° like the mini-modules. The

TABLE 4.1: Experimental setup parameters.

I_{SC}	V_{OC}	**BF**	**PCCE**	**Inclination**	**Height**	**Orientation**
9.3 A	730 mV	90 %	22.7 %	35°	55 cm	South

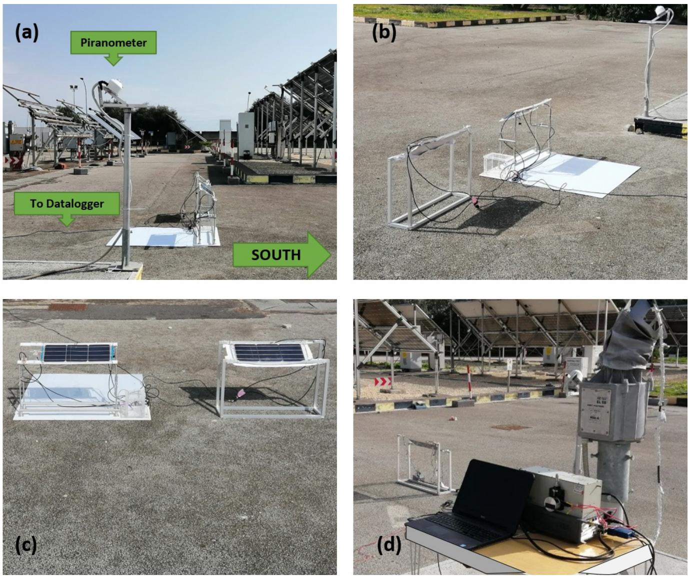

FIGURE 4.1: Pictures of the experimental setup. (a) Westside view of the setup and in foreground the solar irradiance measurement system.(b) Rear and (c) front view of the minimodules.(d) Solar spectrum measurement system.

solar spectrum was monitored with a spectrophotometer. The current-voltage (I-V) characteristics of both mini-modules have been measured in a Kelvin configuration simultaneously and independently. The current is evaluated by the voltage drop across a known resistor in series to the MM and the BM, respectively. The voltage across the mini-module is swept by a variable load, obtained by a powerMOS driven from OFF to ON condition. All the sensors' data were acquired through a National Instrument data logger. Two conditions of ground albedo were studied: asphalt and a white plastic sheet (WPS), as shown in figures 4.1b and 4.1c.

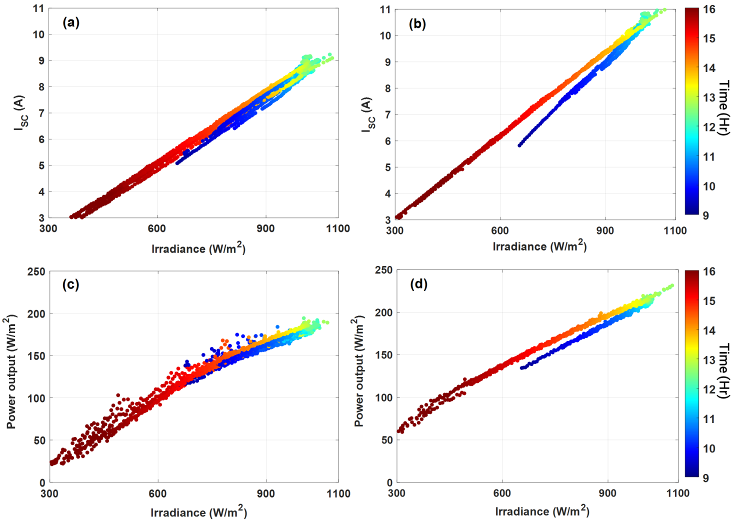

FIGURE 4.2: Isc as a function of irradiance for MM (a) and BM on WPS (b); Power output as a function of time for MM (c) and BM on WPS (d).

4.2 Irradiance effect on electrical output I_{sc} and power output

4.2.1 Effect on I_{sc} and power output

Figure 4.2a and figure 4.2b show cumulative data of I_{sc} collected over the measurement period as a function of irradiance and daily time for MM and BM on WPS, respectively. I_{sc} increases with the solar irradiance, but the MM has lower values under the same solar irradiance, with a difference of about 2 A. Besides, while the MM shows no difference in I_{sc} between morning and afternoon, the BM is characterized by higher I_{sc} values in the afternoon; this effect is even more visible with the WPS owing to its high albedo.

Figure4.2c and figure4.2d show the power output as a function of irradiance for MM, BM on WPS. As expected, the power output of the MM is lower than the BM output. Similarly to what has been observed for the I_{sc}, the BM power versus irradiance graphs shows the same difference in values between morning and afternoon. A noticeable drop in power output for the MM in the afternoon is observed. This is due to the sunlight's low angle of incidence. On the contrary, the BM harvests

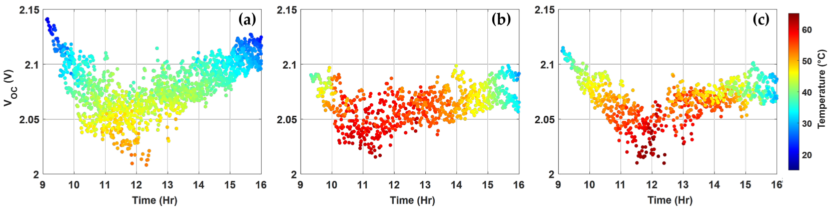

FIGURE 4.3: V_{oc} as a function of time for MM, BM and BM on WPS (d, e and f respectively).

the albedo irradiance on its rear face, therefore producing more power and for a longer time.

The I_{sc} difference results from the cooperation of two effects: the ability of bifacial modules to collect diffused light from the ground and the behavior of the solar spectrum during the day.

4.2.2 Effect on V_{oc}

The temperature difference between the modules perfectly explains the different behaviour in terms of V_{oc}, as shown in Figures 4.3(a,b,c). As expected, the V_{oc} is high in the morning and late afternoon, when the modules are cold, and it is low at noon when the modules are hotter. The MM generally shows the highest V_{oc} value (2.15 V) and the lowest module temperature (20 °C). Figures 4.3 (b) and (c) show how the temperature adversely affects the V_{oc} of the BMs: the BM on asphalt (Figure 4.3 (b)) exhibits a more constant trend of V_{oc}, ranging from 2.02 V to 2.1 V; the BM on WPS (Figure 4.3 (c)) has the lowest V_{oc} (2 V) and the highest temperature at noon. Furthermore, both BM configurations have never surpassed the V_{oc} of the MM.

4.2.3 Albedo influence on module performance

To investigate the first contribution, the albedo was measured, for this particular case defined as the ratio of the photocurrents detected by two calibrated silicon solar cells, one facing up, towards the sky, oriented like the PV modules, and the other exactly parallel, but facing down, seeing the ground. Data collected during one day are reported in figure 4.4, showing that the ratio is higher in the afternoon. This effect arises from the consideration that the reflectivity of asphalt is prominently high in infrared region [55], and the solar spectrum shifts to a

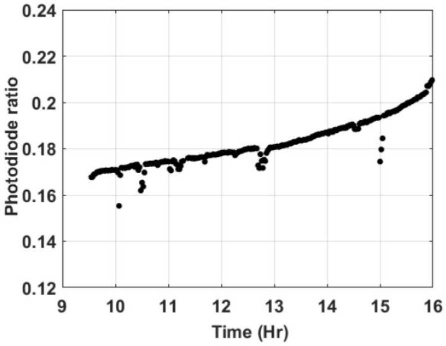

FIGURE 4.4: Ratio of the intensities registered by the photodiodes over one day.

higher wavelength in the afternoon. Therefore, the light impinging on the back side of the BM in the afternoon is higher than at midday and this causes the BM to produce higher currents in the afternoon given the same frontal irradiance, as observed.

4.2.4 Solar spectrum evolution

As previously anticipated, the time evolution of the solar spectrum was acquired during the daytime. Figure 4.5 shows how the central spectrum wavelength (CSW), calculated as the average wavelength weighted by the solar spectrum intensity, increases in the afternoon. There is a clear variation of the solar spectrum shape during the day. The trend is almost symmetrical with the center at noon but shows a rapid increase after 3 pm. The CSW reaches its maximum of 728 nm at 4 pm, with a difference of over 40 nm compared to noon.

The redshift is expected to increase efficiency based on the responsivity of the SHJ cells. The produced current per impinging watt rises with the radiation wavelength and it reaches its maximum at 1030 nm. These data explain the increase of module efficiency in the afternoon, when more infrared photons contribute to the module output, as demonstrated in 4.5. The effect is even more robust in the BM than the MM because the former absorbs light from both sides of the cells.

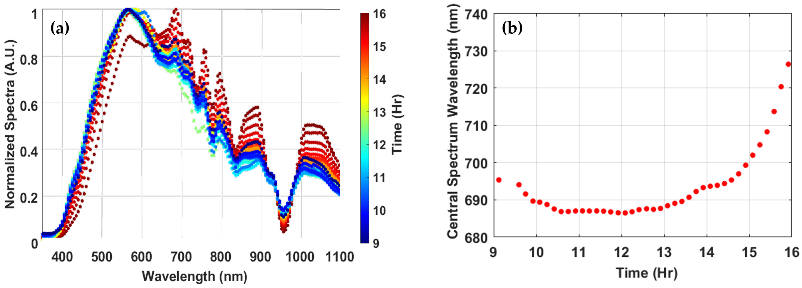

FIGURE 4.5: Daily evolution of solar spectrum (a) and the mean central wavelength of the solar spectrum during the day (b).

Chapter 5

Bifacial photovoltaics and membrane electrolyzer as highly efficient solar hydrogen production system

5.1 State of art

Mitigating climate change urgently requires the adoption of renewable energy, CO_2 sequestration and carbon-neutral energy technologies. Amongst these, photovoltaics is becoming one of the most important. PV energy prices are now highly competitive compared to conventional fossil fuel sources, but the intrinsic randomness of solar power due to the day/night cycle, geographical location, and seasonal variations, etc poses problems. A very promising approach, to solve these complications, is that of solar fuels, i.e., the production of carbon-neutral fuels using solar energy, such as H_2 by means of water electrolysis. For this purpose, one possible solution is a photovoltaic system with suitably designed electrochemical cells (EC), possibly avoiding external electronics to match PV and EC, to decrease costs and increase system reliability [30].

To achieve a large-scale deployment, the cost of solar hydrogen generation must still be significantly reduced. Some figures of merit that can be used to estimate H2 generation costs are solar-to-hydrogen efficiency (STH) and H_2 flow per unit area of a PV cell. Very recently, a record STH efficiency [74] of 30% was reported through the use of a concentrated triple-junction solar cell made of InGaP, GaAs and

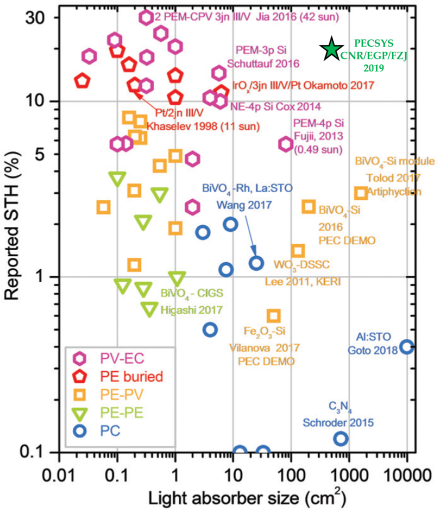

FIGURE 5.1: Device's light absorber's geometric size with reported STH [81].

GaInNAs and a polymer electrolyte membrane electrolyser cell (PEM-EC) with Pt and Ir catalysts operating at 80 °C with a solar concentration of 42 SUN. Other remarkable results with comparable approaches have also been obtained by other research groups [75–77]. To reduce H_2 production costs, one approach is to use silicon-based solar modules instead of a multi-junction solar system. More recently, c-Si modules and Silicon Heterojunction solar cells have been implemented in solar-hydrogen devices [78, 79]. SHJ have been connected to an alkaline electrolysis system with Ni foam electrodes operating under basic electrolytes (1 M KOH), as well as to a PEM-EC system containing Pt and IrOx catalyst coatings on a 177 um-thick Nafion membrane [80]. With both systems, by illuminating a PV area of 5.7 cm2, under a solar simulator at 1000 W/m^2, an STH efficiency of 14.2% has been demonstrated. Figure 5.1 report several STH records of technologies and setups used for hydrogen generation taking into account the area of light absorber [81], the star represents the achieved goal of the PECSYS project. In the last few years, the Si PV research community has paid ever more attention to the development of bifacial Si PV modules. With this technology, a PV module collects sunlight from both the front side, by collecting the albedo radiation diffused by the ground, producing a noticeable increase in the PV energy yield. For this reason, the problem of the optimization of the bifacial module installation is widely investigated in the literature and the PV community, as it holds great promise for the further improvement of PV technology [46–49, 82–85].

5.1.1 Experimental setup

In the interest to reduce the voltage drop across the wiring, the PV mini-module is directly coupled to the PEM-EC cell through the use of low-resistance copper cables. The current flowing through the system is evaluated with the voltage drop across a 1.30 m Ω resistor in series. Meanwhile, the horizontal solar radiation is evaluated using an MS-40 EKO pyranometer, while the solar radiation at the PV module tilt angle orientation is measured by a calibrated Si reference PV cell. All the data are acquired through a CR1000 Campbell Scientific data logger and analysed by data treatment software (Matlab®). Figure 5.2a and b display a schematic drawing and picture of the system, respectively. The PEM-EC is operated at ambient pressure and low temperature of less than 40 °C.

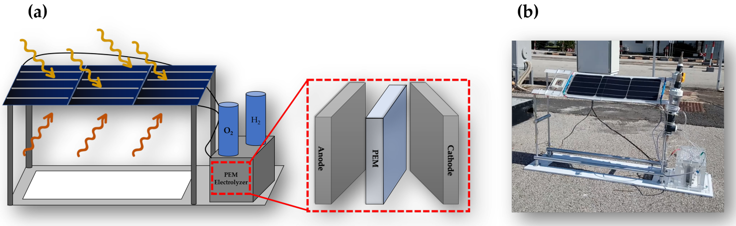

FIGURE 5.2: (a) Schematic of the coupled PV-PEM-EC system and (b) picture of the system.

Under these conditions, the Faradaic efficiency was considered about 100% [86], for this reason, the H_2 flux is evaluated by the instantaneous electrical current flowing in the system. The water is stored in an atmospheric open tank with a volume of 300 mL. Water is supplied to the EC device via 6mm PTFE tubing and an active water circulation system has been avoided as unnecessary. Hydrogen and

Oxygen in this experiment are not stored but are released into the atmosphere.

5.1.2 PEM-EC design

The PEM-EC system, made by the Jülich research centre, is composed of different functional layers that ensure a good media supply to the electrochemically-active layers, a relatively high power density and high efficiency. The cell itself consists of flow field structures made of expanded carbon material, which is machined utilizing water jet cutting. The diffusion layer is in contact with the flow structure and has a porosity of 80% and electrical conductivity. The electrochemically active layer is made of a mixture of Nafion and Iridium, with a catalyst loading of 2.7 $mgcm^{-2}$ Ir at the anode. At the cathode, platinum is the catalyst material and catalyst loading is 0.7 $mgcm^{-2}$ Pt. The electrochemically active layers are in contact with a Nafion HP membrane with a thickness of 20 μm. The electrodes area is 10 cm^2.

5.1.3 Optimal bifacial conditions determination

Bifaciality requires optimization to take full advantage of the ground albedo radiation. Based on a model created previously and described in [54, 57], it was possible to predict bifacial solar module installation optimization, based on the numerical evaluation of the photocurrent collected by the backside of the bifacial solar cell. Briefly, the model is based on the evaluation of the solid angle under which each ground element sees the solar cells taking in account the isotropically diffuses horizontal solar radiation incident on the element reduced by the normal incidence reflectivity of the ground. Furthermore, the model includes the wavelength (λ) dependence of the external quantum efficiency of the solar cell. EQE and detector responsivity was acquired through Bentham PVE 300, in the range from 300 nm to 1100 nm, and used for the model calculation. Figure 5.3 shows both the responsivity and EQE of a single SHJ cell, from both sides. The electrical response per impinging watt rises with the radiation wavelength and reaches its maximum at 1030 nm.

Considering, the latitude and longitude of Catania-Passo Martino (37°240N, 15°10E), where the experiments have been performed and applying the model in this context it was possible to evaluate the best

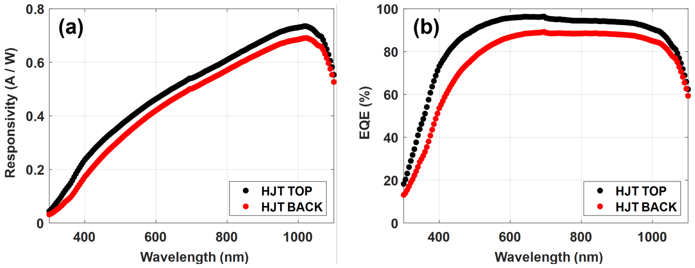

FIGURE 5.3: Spectral responsivity (a) and external quantum efficiency of both front and back side of SHJ solar cell.

possible bifacial PV system design to drive a water-splitting PEM-EC cell. Figure 5.4a and b report the daily energy yield calculated by the model taking in account two parameters the inclination (tilt angle) of the module concerning the horizontal plane and the module's height.

In figure 5.4a, a clear maximum is evident at approximately 35–40°, close to the local latitude. This is in good agreement with the evaluations of [87] for monofacial PV systems. From figure 5.4b, it is evident that at a height above 40 cm, the energy yield increase drops. Therefore, based on the results of figure 5.4a and b and of the above considerations, the PV system has been designed by using three cells organized in one row, with a 35° tilt angle and a 50 cm module height. Figure 5.4c reports the daily energy yield of the horizontal three-cell PV system with a 35° tilt angle and 50 cm height as a function of the average ground albedo. The zero albedo corresponds to the monofacial energy yield. The PV energy yield increases with the albedo. In our experiment, the average albedo (α) is 30%, so the expected PV energy yield increase, compared to the monofacial system, is +13.6%. Moreover, as the albedo increases, the expected energy yield increase (YAF) is about +6 Whr per m^2 and per % albedo, equal to +0.45% per % albedo.

5.1.4 Effect of bifaciality on hydrogen production

To better understand the effect of bifaciality on the system, two configurations were tested. The monofacial module is the same bifacial PV module, but with an added white sheet placed on the module's backside to shield the back-side illumination from the ground albedo.

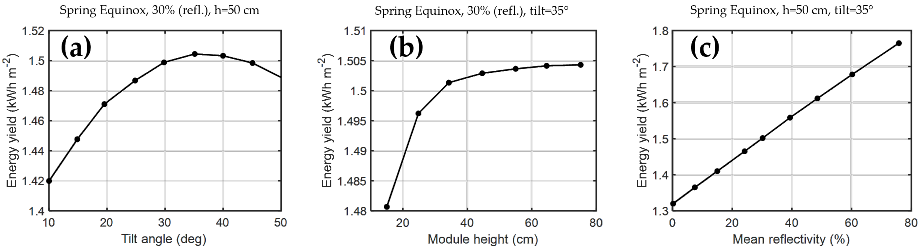

FIGURE 5.4: Daily energy yield: (a) with an average ground albedo of 30% as a function of module inclination (tilt angle), constant height of 50 cm; (b) with an average ground albedo of 30% as a function of module height at a fixed tilt angle of 35°; (c) of a three-cell PV module with a 35° tilt angle and 50 cm height as a function of the average ground reflectivity.

Before setting up the demonstrator the current-voltage characteristics of the system was performed components. Figure 5.5 shows the current-voltage (I–V (a)) and power-voltage (P–V(b)) characteristics, that is the PV mini-module, and the PEM-EC cell, acquired in standard conditions obtain by the solar simulator (25 °C and 1000 $Wm^{-}2$ incident solar radiation). Bifacial and monofacial characteristics are shown as red and black solid lines, respectively.

The PV module efficiency (ηPV) is defined as the ratio between the module maximum electrical power Pmpp, shown in Fig. 4(b) and the incident solar optical power (corresponding to an optical power density Pin). For P_{in} = 1000 Wm^2 the obtained efficiency value ηPV for the PV mini-module operating in monofacial mode is 16.4%, calculated as:

$$\eta_{PV} = \frac{P_{mpp}}{N \cdot A \cdot P_{in}} \tag{5.1}$$

where N is the number of cells in the mini-module for this system equal to 3 and A is the cell area (243.36 cm2). The bifacial module shows a +12% increase of power in the MPP, and therefore of the effective efficiency, compared to the monofacial module, which is in good agreement with the simulations shown in figure 5.4. 3 (ground with about 30% average albedo). The characteristics of the PEM electrolyzer at 25°C are shown in Fig. 3 (a) and (b) as blue lines. In general, the operating point of the EC-PV system, defined by the couple (Vc, Ic), is obtained as the intersection of the EC cell and PV

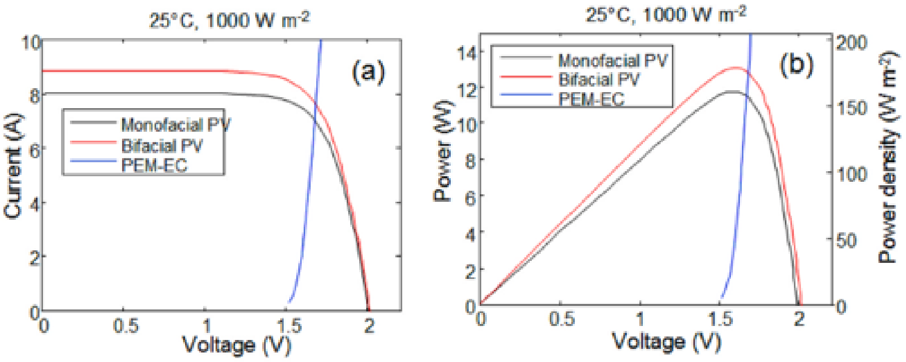

FIGURE 5.5: (a) Current-voltage characteristics of the three-cell PV module in monofacial and bifacial operation and of the PEM electrolyzer; (b) power-voltage characteristics of the three-cell PV module in monofacial and bifacial operation and of the PEM electrolyzer. The right axis shows the corresponding PV module power density.

module I–V curves, as visible in Fig. 3(a). Then, the STH efficiency is defined as:

$$STH = 1.23 \cdot I_c \cdot \frac{\eta_F}{N \cdot A \cdot P_{in}} \tag{5.2}$$

Assuming a 100% faradaic efficiency (ηF) as discussed above, for a given PV module with short circuit current ISC, the maximum achievable STH is:

$$STH_{max} = 1.23 \cdot \frac{I_{sc}}{N \cdot A \cdot P_{in}} \tag{5.3}$$

In particular, from the data shown in figure 5.7(a) and (b), the STH_{max} is equal to 13.7% in monofacial mode. For the EC cell the I–V curve can be approximated to a linear relationship, that is:

$$V_c = V_{th} + R_{ec} \cdot I_c \tag{5.4}$$

where Vth is the threshold voltage above which the EC current is larger than zero, and R_{ec} is the EC cell series resistance. In the present experiment V_{th} = 1.55 V and R_{ec} = 13 mΩ, therefore Vc is approximately at the PV module maximum power point, i.e. Vc =

Vmpp = 1.65 V. Figure 5.6 shows that the expected STH is about 90% of STHmax, confirming the system designed and the good match between EC and PV-module.

Figure 5.7 presents the comparison of H_2 flux (a) and STH (b) of the same system operating in bifacial and monofacial mode, measured outdoor from approximately 9 a.m. to 4 p.m. The data were measured on two different days with the same system (except for the use of the white sheet on the PV module's backside in the case of monofacial operation).

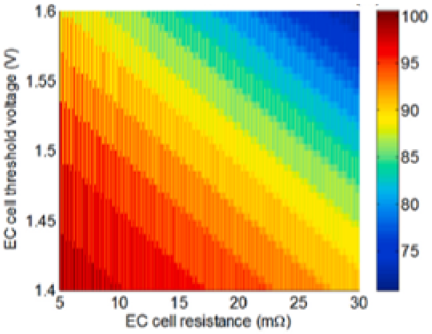

FIGURE 5.6: Ratio between the calculated STH value at Vc and the maximum STH, STHmax, as a function of the EC cell resistance REC and of the EC threshold voltage VTH.

The solar irradiation conditions (reported in Figure 5.7(a)) were measured through the calibrated Si reference cell. It is evident that during bifacial operation, the H_2 flux and STH efficiency were larger, with an average increase to the STH efficiency obtained with the monofacial system, of 14.7% and 12.2% between 11 a. m. and 2 p.m., respectively. Such a noticeable difference is attributed to the effective collection of albedo radiation from the ground by the bifacial PV system. Noteworthy is that such an H_2 flux production increase is achieved with no extra equipment, such as the mirrors of Fresnel lenses for solar radiation concentration, with the possibility to increase the performance with a simple white panel. Indeed, figure 5.7(a) reports the comparison of the bifacial PV-EC system operating simply with the ground albedo due to only the asphalt (See figure 5.8a), or with an increased albedo due to the addition of a $1m^2$ plastic white panel placed on the ground below the PV module.

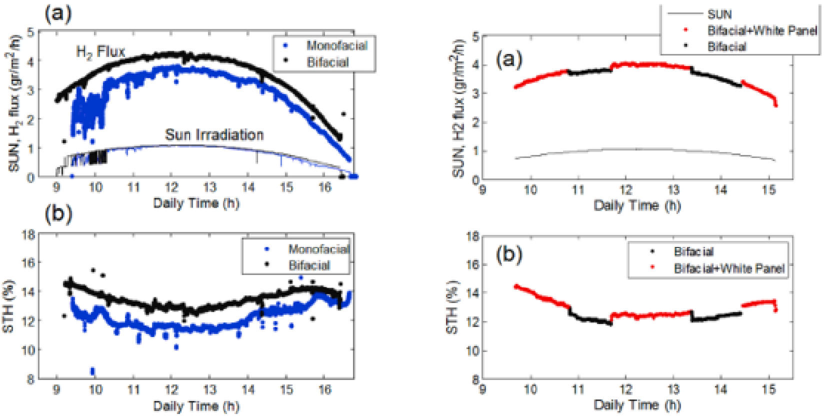

FIGURE 5.7: (a) Solar irradiation conditions (SUN) and H_2 flux per unit PV area, measured during outdoor operation in a bifacial or monofacial configuration. The same system was tested on two different days, exhibiting similar solar irradiation and weather conditions: (b) comparison of the STH efficiency.

Figure 5.8a shows the reflectivity as a function of wavelength measured for the asphalt and the white panel. The experimental setup is shown in figure 5.8b. As the average albedo with the white panel is 53%, against the value of 30% of the asphalt, according to the simulation in Fig. 3(c), the yield increase should be the YAF times the albedo increase, equal to +20%, which is a total of 0.45 X 20 = 9% expected yield increase. As shown by the data in figure 5.7, the increased albedo obtained with the white panel on the ground produces an increase of H_2 flux and an STH efficiency of about 5.5%, to the bifacial panel results.

The experimentally derived value is lower than expected from the model, but this is reasonable, as the albedo increase is only partial, given the limited dimension of the white sheet ($1m^2$) used for the experiments. Nevertheless, the results indicate that higher ground albedo can effectively increase the hydrogen production yield.

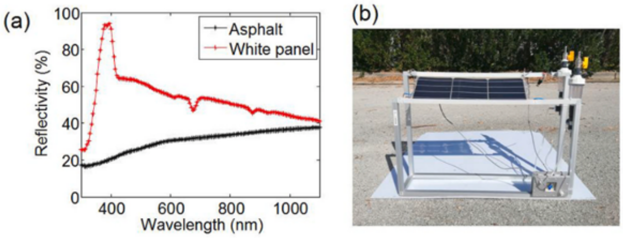

FIGURE 5.8: (a) Reflectivity versus wavelength of the asphalt and of the white plastic panel; (b) picture of the experimental setup, using the 1 m^2 white plastic panel on the ground.

5.1.5 Long term stability

Figure 5.9 shows the experimental results taken on the system on eight different days. H_2 flux, STH Efficiency and solar irradiation data, together with the average daily temperature are reported in the figure. As it is evident, weather, temperature and solar irradiation conditions varied across a wide range of values, as can be seen from an inspection of the data of figure 5.9 . Nevertheless, no appreciable change of STH efficiency was observed for a total operation time of about 55 h, indicating that the proposed approach is promising in terms of performance and endurance.

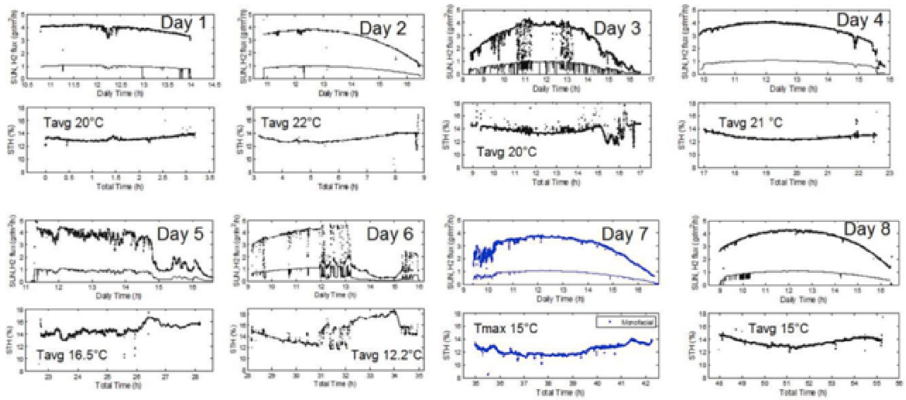

FIGURE 5.9: Solar irradiation conditions (SUN), H_2 flux per unit PV area and STH efficiency measured during outdoor operation for eight days, with a total operation of more than 55 h, without efficiency degradation.

Chapter 6

Improved Fe-based catalysts for Nitrogen reduction reaction

6.1 Introduction

As stated in the introduction ammonia is not only an important chemical, largely essential in agriculture as fertilizer, as well as for plastics and pharmaceuticals, but it is also a promising energy vector, because of its high hydrogen content, high volumetric energy density and easy of liquefaction for storage [18, 88–90]. Industrial production of ammonia mainly relies on the well consolidated Haber-Bosch process, that requires high temperatures (350-550°C) and high pressures (150-350 atm) to make efficient the reaction between nitrogen and hydrogen gases ($N_2 + 3\,H_2 \longrightarrow 2\,NH_3$, $\Delta f H0$=-91.8kJ mol^{-1}) and it is responsible for massive CO_2 generation, roughly corresponding to about 2% of worldwide emissions [91, 92]. Nitrogen reduction reaction to ammonia obtained through electrocatalytic processes is considered an interesting alternative since it offers the possibility of directly using water as hydrogen source and can be conducted at ambient temperature and pressure [93, 94]. Despite the great interest and the efforts that have been made to improve the ammonia formation yield rate, the electrochemical synthesis of ammonia is still at a nascent stage and it faces many drawbacks [95]. The e-NRR mechanism is quite complex and still unclear, even if many efforts have been devoted to the elucidations of its highlights.

Basically, it consists of three steps:

1. N_2 adsorption at the active site.
2. Hydrogenation.
3. Desorption of the NH_3 molecule from active sites.

Once the N_2 approaches the surface, different paths are possible according to the predictions already present in the literature and based upon the breaking of the $N\equiv N$ triple bond, discussed in chapter 2. The most mentioned in literature are the dissociative and the associative mechanisms. In the former the triple bond is broken during adsorption on the catalyst site, so, after hydrogenation, the surface is populated by NHx species. In the associative pathway, instead, the N_2 molecule is broken after adsorption during the hydrogenation process and the catalyst sites are covered in principle with N_2Hx species as discussed in the chapter 2 [96, 97]. Furthermore, for both cases hydrogenation could occur following a) Tafel type mechanism, with protons first adsorbing on the surface, it combines with electron and then reacts with adsorbed N-type species or b) Heyrovsky type reaction where the N-type species directly bond with protons from the solution and electrons from the electrode [97]. The latter is the most widely accepted approach since the Tafel model is considered extremely sluggish.

However, the stability of the covalent N_2 bond typically shifts the potential required for e-NRR to regions where the protons reduction to H_2 is favored. Therefore, one major challenge for nitrogen reduction is the low selectivity due to the competing hydrogen evolution reduction. This usually determines low faradaic efficiency for nitrogen reduction, since a largest number of electrons is used for hydrogen evolution, whilst only a small fraction is used for reducing nitrogen. To overcome the selectivity challenge, an optimal catalyst should be able to enhance the e-NRR activity and suppress the activity of the competing HER. Theoretical studies based on Density Functional Theory calculations provide predictions on catalysts materials and morphology, such as the effects of defects, facet and surface functionalization [98–102].

6.2 State of art

Recent works have demonstrated the potentiality of noble metals such as Au, Rh and Ru for the e-NRR reaction, with yield rate up to about $6gh^{-1}cm^{-2}$ for Ru and faradaic efficiency of 13.36% for Au, with a top NH_3 yield rate of $9.43h^{-1}mg_{cat}^{-1}$ [94, 103–108]. However, the use of earth abundant catalysts would be preferable because their availability. Transition metal based materials, for example, offer an compelling alternative: whilst non precious, they would be desirable for a sustainable and circular economy [109, 110]. In addition, they seem very promising for e-NRR, thanks to the presence of d orbital electrons and unoccupied orbitals suitable for activating the strong $N\equiv N$ triple bond [111, 112]. The e-NRR mechanism associated to the TM materials is the associative Heyrovsky model, with catalytic sites populated by N_2Hx species [97]. Among low-cost materials, Fe-based catalysts have received attention because of the high activity. Iron is abundant and it also plays a key role in biological nitrogenase for natural N_2 fixation, so there is growing interest in Fe based catalyst and its oxides where the intrinsic HER activity could be suppressed. For instance Fe/Fe_3O_4, Fe_3O_4/Ti have shown Faradaic efficiencies of 8.29% and 2.6% and rate of $0.2\mu gh^{-1}cm^{-2}$ or $3.42\mu gh^{-1}cm^{-2}$, respectively [110, 113, 114]. Single atom catalysts (SACs) made of isolated single Fe atomic sites anchored to N-doped carbon frameworks have shown a yield rate of $62.9\mu gh^{-1}mg_{cat}^{-1}$ [115]. Recently, also Fe_2O_3 has been investigated as an active catalyst material in a molten hydroxide water electrolysis cell where NH_3 was directly synthetized at 200°C and 25 bar achieving a faradaic efficiency of 35% [116]. However, high temperature electrolysis requires high power supply and complex facilities, making it less compatible with renewable energy sources. With the aim to perform the electrochemical synthesis of ammonia at low temperature, several Fe-based catalysts with different chemical states have been analyzed and the results show that the manipulation and engineering of the surface states by changing the morphology is a good strategy to provide active sites and promote interactions between electrocatalysts and gas, allowing a gain in the Faradaic efficiency if compared to untreated Fe surface [117].

6.2.1 Experimental

The experimental apparatus and procedure are described in figure 6.1. A rigorous protocol was adopted to remove the external contaminations widely discussed in the literature [118–121]. Before chronoamperometry experiments, both cell and electrodes were washed at 35°C in water while stirring the solution for 30min.

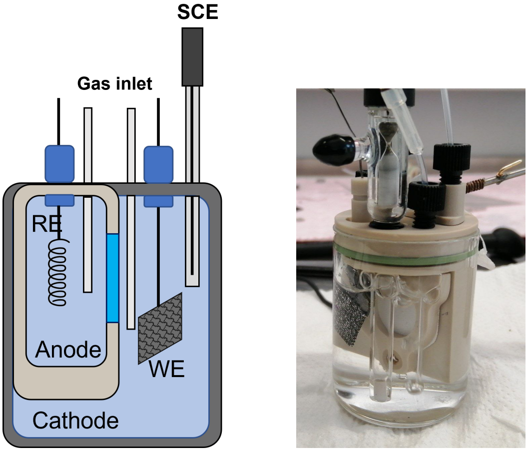

FIGURE 6.1: Scheme of the electrochemical cell in operation.

N_2 and Ar (Nippon Gases 99.9999%) were purified by going through three gas washing bottles, placed before the cell, two of which were filled with 10mM H_2SO_4 while the third contained only water. An additional acidic trap was placed after the gas outlet. The electrolyte was analyzed before experiments (time T0), then the cathode and the anode compartments were filled respectively with 22ml and 8ml and they were measured again the solution after 10min (time T1) and 40min (time T2) at the open circuit and with nitrogen flow, to detect the ammonia already present in the cell, if any. If the NH_3 concentration was more than $10^{-6}M$ and/or it changed with time, the cell was emptied and rinsed again. This approach allowed a careful investigation of the possible contaminations originating inside the system, e. g. ammonia already present on the electrode surface or in the cell. The quantity of ammonia presents at the open potential was subtracted from those measured after experiments with external voltage applied. The same measurements were done on both anodic and cathodic compartments but no NH_3 increase was detected at the anode. Ar-saturated control experiments were performed at the same bias or with inactive catalysts as recommended in the literature [117].

6.2.2 Ammonia Quantification

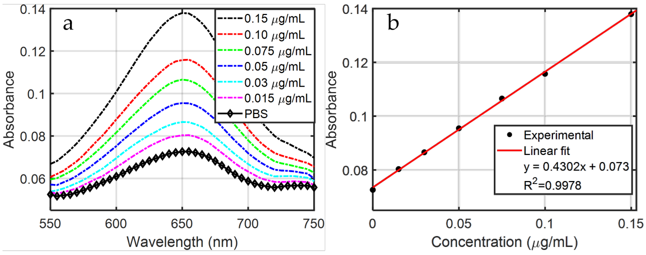

FIGURE 6.2: (a) UV-Vis absorbance spectra for the indophenol procedure with various NH_4^+ con-centration ranging from $0.015 \mu gmL^{-1}$ to $0.015 \mu gmL^{-1}$ in PBS solution. (b) The corresponding calibration curve.

The amount of ammonia in the solutions was measured based on the indophenol blue method reported by Di Zhu et al. with slight modifications [102]: 1 mL of the electrolyte was mixed with 1 mL of a mixture solution consisting of NaOH (1 M), sodium citrate (5wt%), and salicylic acid (5wt%), followed by adding 0.5 mL of a NaClO solution (0.05 M) and 0.3 mL of a sodium nitroferricyanide solution (0.1wt%). The obtained mixture was kept for 30min in the dark to prevent the Fe-catalyst photodegradation. The absorbance of the solution was detected at $\lambda = 655$ nm through an ultraviolet-visible (UV-vis) spectro-photometer (Bentham PV300) [122]. To calculate the amount of produced NH_3, the calibration curve was fitted using standard ammonia chloride solutions, prepared in PBS electrolyte solution in the range between 0.15 and 0.015 μgmL^{-1} as reported in figure 6.2.

6.2.3 Catalyst Preparation

For the catalyst synthesis several aqueous solutions were prepared with 1 mM, 2 mM and 10mM of $FeCl_3$ (anhydrous, powder, $\leq 99.99\%$ from Sigma Aldrich). A drop of 0.6ml of each solution was placed on carbon cloth (AV Carb 1071 HCB) substrates (3 x 1.5) cm^2 on a hot plate at 80°C. After water evaporation, substrates covered with the $FeCl_3$

powder were treated in $NaBH_4$ (powder, $\leq$ 98.0% from Sigma Aldrich) 100mM for 60s, at 21°C while stirring the solution at 200rpm. The Fe ions is reduced into elemental Fe on carbon cloth surface by $NaBH_4$ according equation C 6.1 generating iron nanostructure.

$$Fe^{3+} + NaBH_4 \longrightarrow Fe^0(s)\downarrow + H_2(g)\uparrow + B(OH)_3 \qquad (C\,6.1)$$

After this step, samples were abundantly rinsed in deionized water and dried with air. Some samples were also annealed at 250°C in air for 2h.

6.2.4 Electrode characterization

For the morphological, structural and chemical analyses a Scanning Electron Microscope (SEM) ZEISS SUPRATM 35 was adopted. The same deposition procedure was replicated on a carbon grid for Transmission Electron Microscope (TEM) analyses with JEOL 2010F, equipped with a spectrometer GIF 2001 for electron energy loss (EELS) spectrum imaging and bright field (BF) / high angle annular detector (HAADF) for wide angle diffraction. The electrochemical measurements, both cyclic voltammetry and chronoamperometry , were carried out in a standard two compartments electrochemical cell using a Pt wire as counter electrode (CE) and a saturated calomel electrode as reference. The conversion to the RHE reference scale is obtained using the following equation:

$$E_{(vsRHE)} = E_{(vsSCE)} + 0.243 + 0.059 \cdot pH \qquad (6.1)$$

The cathodic and the anodic compartments were separated by a ZIRFON PERL membrane (AGFA) [120] and filled with 22ml and 8ml respectively of 0.01M phosphate buffer solution as electrolyte (PBS tablets by Fisher Scientific). Measurements have been performed by using a Keithley 2600-Source Current Unit.

6.2.5 Result ans discussion

Figure 6.3(a-b) and (c-d) shows the SEM micrographs of the carbon cloth electrodes obtained with 1 and 2mM $FeCl_3$ respectively. Very small particles can be seen at high magnification in figure 6.3(b). The mean size is about 38nm and they cover 30% of the electrode surface.

When the $FeCl_3$ concentration increases, the particles size increases too and coalescence produces an interconnected metal network, as it can be seen in Figure 6.3(d); the corresponding covered area is 55%. High surface homogeneity emerged for the deposition with the more concentrated solutions, marked by a resulting smooth catalyst layer. Similar results were obtained after annealing the 1mM $FeCl_3$ sample in air at 250°C for 2h and with 10mM $FeCl_3$.

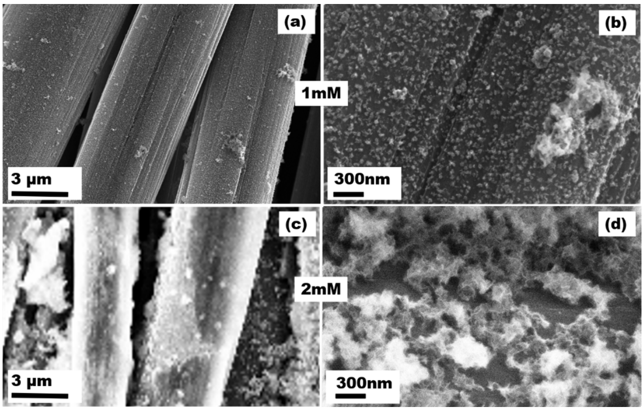

FIGURE 6.3: SEM micrographs at low and high magnifications of the AV Carb samples after deposition in $NaBH_4$ and (a-b) 1mM, (c-d) 2mM $FeCl_3$ respectively.

The electrochemical active surface area was evaluated, by cyclic voltammetry method and under Ar flux. In a non-Faradaic region, a series of CV scans at different rates were acquired, the double layer capacitance (Cdl), directly related to the EASA, was computed from the slope of the linear regression between the current density differences (cathodic and anodic) in the middle of the potential window of CV curves versus the scan rates [123]. Results are shown in figure 6.4. The electrochemical analysis showed that a superior catalytically active surface area is associated to the electrode with the smallest particles size (deposited with 1mM $FeCl_3$). Increasing the $FeCl_3$ concentration in the solution has no advantage in terms of active electrochemical sites, as well as the annealing of the sample.

The deposition procedure of 1mM-Sample was replicated on a TEM C-grid and the nanoparticles were analyzed. Figure 6.5a shows the EELS spectra acquired on two regions of the sample. In the area under

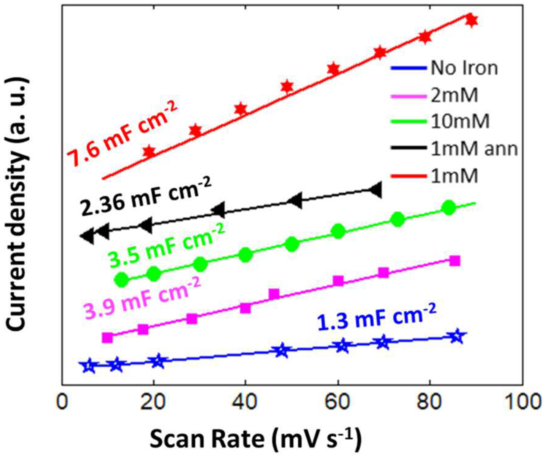

FIGURE 6.4: Double layer capacitance calculated from cyclic voltammetry for the AV Carb samples loaded with Fe-based catalyst.

investigation, It has been found that the shape of the L3 edge of Iron changes locally. In region 1 the shape of the EELS spectrum can be typically ascribed (figure 6.5 b) to Fe_2O_3 with two peaks, one at 709.3eV, attributed to a change in the oxidation state, and one at 710.8eV, more intense [124]. In region 2 instead, the spectrum exhibits a single peak at 710 eV, related to Fe_3O_4. Both Fe_2O_3 and Fe_3O_4 were deposited on the sample. Figure 6.5 c shows HRTEM acquired on a particle of region 2, showing the (222) and (400) crystalline planes of Fe_2O_3 with corresponding d-spacings of 0.48nm and 0.208nm respectively while in figure 6.5 d is reported the HRTEM but on a Fe_3O_4 particle, together with the corresponding FFT showing the (111) and the (220) diffraction spot, with a d-spacing of 0.25nm and 0.29nm respectively [125, 126].

The presence of both Fe_2O_3 and Fe_3O_4 in the 1mM-Sample deposited on carbon cloth is confirmed by XPS analyses. Figure 6.6 shows Fe 2p peaks of as deposited 1mM sample. The catalyst is a mixture of Fe_3O_4 and Fe_2O_3, since peak 1 is related to Fe^{2+} of Fe_3O_4, peak 2 is typical in the Fe^{3+} of Fe_2O_3, peak 3 also is a satellite peak associated with Fe_3^+ of Fe_2O_3 [109, 127, 128].

The reduction of a part of Fe^{3+} to Fe^{2+} produces oxygen vacancies,

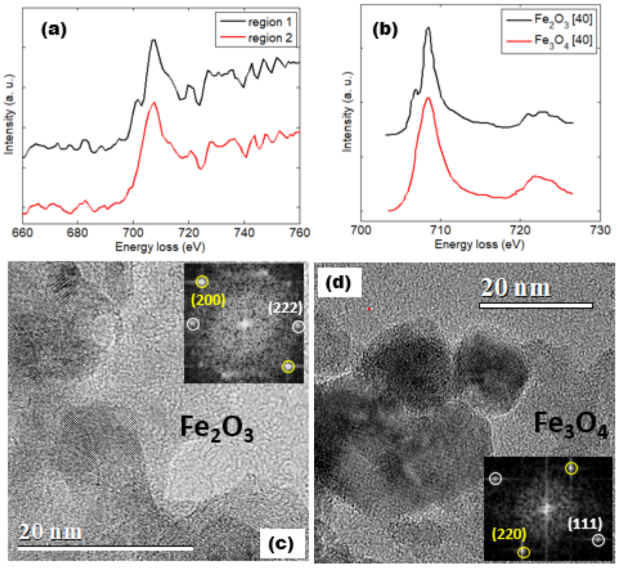

FIGURE 6.5: TEM analyses on nanoparticles obtained in the 1mM $FeCl_3$ solution, (a) EELS spectrum for the L3 edge of Iron acquired in two distinct regions of the TEM specimen and (b) literature data from [124]; (c-d) high resolution TEM on nanoparticles in regions 1 and 2 with the corresponding diffraction pattern [125, 126].

as it can be evidenced by the Oxygen XPS O1s signal (figure 6.6 b), made by the convolution of two peaks, one at 529.9 eV, peak 1, typical of metal oxygen bond, and peak 2, at 531.13, corresponding to the oxygen vacancies [129]. Oxygen vacancies are ubiquitous in metal oxides and have a pronounced effect on the physical and chemical properties of the material. Numerous strategies have been developed to create OVs in metal oxides, such as high temperature calcination, high energy particle bombardment, ion doping or chemical reduction (e. g. from H_2 or $NaBH_4$). The deposition method adopted in this study, including the chemical reduction by $NaBH_4$,is therefore expected to promote the OVs formation, whose presence has been reported to accelerate the charge/electron transfer rate, and therefore improving the electrocatalytic performance [102, 129]. XPS spectra for Fe 2p in the 1mM sample after cyclic voltammetry with data obtained by simulation.

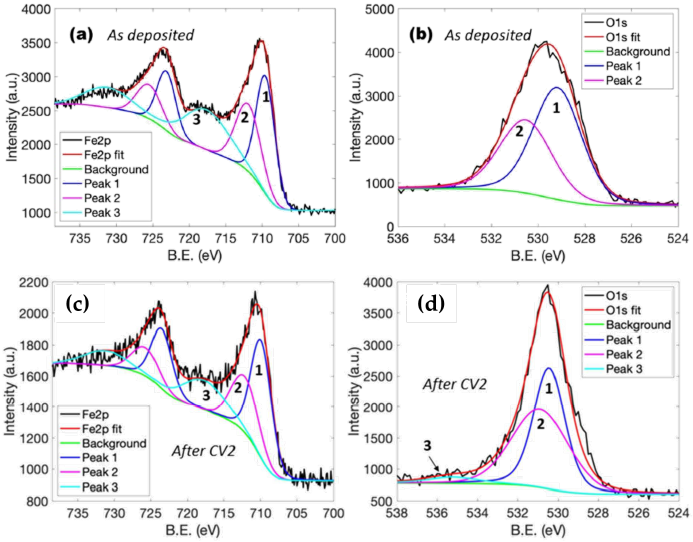

FIGURE 6.6: XPS spectra for Fe 2p in the 1mM sample before (a-b) and after (c-d) cyclic voltammetry with data obtained by simulation.

The catalyst activity and stability were analyzed by cyclic voltammetry (CV), with a scan rate of 15mV s-1 under N_2 flux. Firstly a potential range between 0.07 V and -0.45 V vs RHE was adopted to avoid catalyst modification upon voltage. The corresponding CV is shown in Figure 6.7 (CV1). The voltage was applied according to the arrows, from the less to the most negative in a direct scan (dotted arrow) and vice versa in the reverse one. Each scan was repeated 4 times. Then, chronoamperometry (CA1) at -0.33V vs RHE experiment was started and evaluated the produced ammonia after 40 minutes. During the CA1 the absolute value of the cathodic current initially decreases as a function of time and then increases. The corresponding ammonia yield is 5.5 $\mu g mg_{cat}^{-1} h^{-1}$ with a Faradaic efficiency of 3.8%. A new scan (labeled as CV2 in figure 6.7a) was performed with a wider range, from 0.07 vs RHE to -0.63 V vs RHE. The corresponding voltammogram (CV2) is quite different from that obtained before: the HER reaction seemed to be hampered and in the reverse scan an anodic peak centered at about – 0.05V vs RHE appeared. The CA measurement performed after CV2 (CA2 in figure 6.7b) shows a more stable behavior and a net increase in the ammonia yield rate. Indeed, the measured ammonia rate after CA2 is 26 $\mu g mg_{cat}^{-1} h^{-1}$, with a Faradaic efficiency of 18%, very large compared to the result obtained on the same electrode after CA1, i.e. after cycling in a narrower and less negative voltage range.

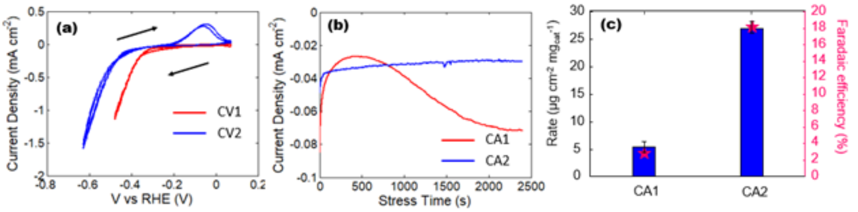

FIGURE 6.7: Electrochemical experiments for ammonia generation in the sample obtained with 1mM FeCl$_3$, (a) cyclic voltammetry obtained scanning the potential from 0.07 to -0.45 V vs RHE (red) and from0.07 to -0.63 V vs RHE (blue), (b) the corresponding chronoamperometry and (c) NH$_3$ yield rate and Faradaic efficiencies at the given potentials.

Such an activation procedure has been also applied to the other samples produced with higher Fe concentration in the deposition solution, obtaining similar results, although with less improvement in the yield. As an example, Figure 6.9a, b and c show the CV, CA and the ammonia yield data, respectively, for the sample treated with 2mM FeCl3 (figure 6.3 (c-d)). After the activation procedure (Figure 6.9 (a-b)) the rate increases from 3.3 to 6.6 µg mgcat-1 h-1 and the Faradaic Efficiency increases from 6% to 12%. No relevant improvement in the yield upon activation has been obtained for 10 mM sample and for annealed 1mM. In both the cases an almost uniform film was obtained at the carbon cloth surface, instead of nanoparticles.

In order to better investigate the activation mechanisms, and to understand if it takes place during the CV2 (with extended range) or the CA1, the catalyst activity has been measured by EASA after CV2 and after CA, performed on a fresh sample, as reported in figure 6.8. The double layer capacitance of the as deposited catalyst, equal to 7.6mF cm-2, increases up to 11.7mF cm-2 after CV2. The CA, performed without being preceded by the CV2, instead, does not produce any significant change. These results clearly indicate that an increased active area can be obtained by the extended

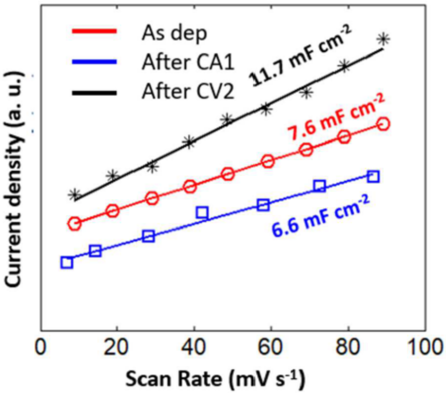

FIGURE 6.8: Comparison of electrical double layer capacitance before and after the CA1 and CV2.

cyclicvoltammetry (CV2), which can then be considered as a suitable activation procedure.

According to the iron Pourbaix diagram[130] (reported in figure A.1), in the negative voltage range, at the cathode side at pH of about 7 two reactions are expected to occur [131]. Indeed, at 0V the most stable compound is Fe_2O_3 Fe^{3+} but it partially reduces in Fe_3O_4 (with Fe^{3+} and Fe^{2+}) at about-0. 15V vs RHE and then in Fe at -0.5 vs RHE.

$$3\,Fe_2O_3(s) + 2\,H^+ + 2\,e^- \rightleftharpoons 2\,Fe_3O_4(s) + H_2O \qquad (C\,6.2)$$

$$E_0 = 0.66V - 0.059 \cdot pH$$

$$Fe_3O_4(s) + 8\,H^+ + 8\,e^- \rightleftharpoons 3\,Fe(s) + 4\,H_2O \qquad (C\,6.3)$$

$$E_0 = 0.085V - 0.059 \cdot pH$$

In order to obtain more insight on the structural changes induced by the activation process XPS spectrum of the 1mM sample after activation and drying were performed. Figures 6.6 c and d show the Fe 2p spectra acquired after cyclic voltammetry in range 2 (CV2). As already seen for the as deposited sample figure 6.6a three peaks are obtained. The fitting data are reported in Table 1of SI. However, after

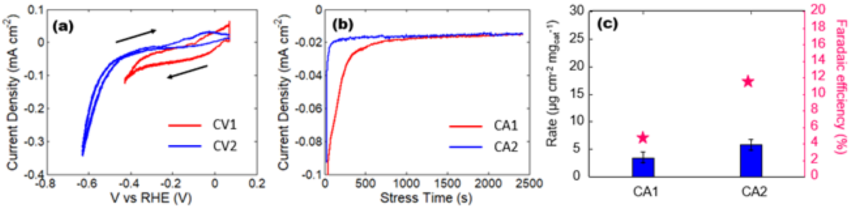

FIGURE 6.9: Electrochemical experiments for ammonia generation in the sample obtained with 2mM FeCl3, (a) cyclic voltammetry obtained scanning the potential from 0.07 to -0.45 V vs RHE (red) and from0.07 to -0.63 V vs RHE (blue), (b) the corresponding chronoamperometry and (c) NH3 yield rate and Faradaic efficiencies at the given potentials.

activation the contribution of peak 1 (Fe+2) increases from 39% to 48%, that of peak 2 (Fe+3) does not change and the satellite area decreases from 32% to 23%, suggesting an increase of the amount of reduced iron and a corresponding increase of the oxygen vacancies after cyclic voltammetry.

The O1s XPS peaks before and after as reported in figure 6.9 activation changed too. The small peak at 535.25eV binding energy (peak 3) is related to surface hydroxyl groups. An increase in the oxygen vacancy peak (peak 1 at 531eV BE), the relative area increased from 41.5% to 49.7%, at the expense of that corresponding to the metal oxygen bond (peak 2 at 530eV BE), with a decrease in the relative area from 58.5% to 46.1% were observed. Such a change improves the electrocatalytic activity of the layer thanks to a new asymmetric three dimensional electronic structure obtained after oxygen removal [129]. It is possible to conclude that (1) the activation process takes place by cyclic in the extended range (+0.07 vs RHE to -0.63 V vs RHE) and (2) the activation produces an increase of the oxygen vacancies and

Fe^{2+}/Fe^{3+} ratio and a corresponding increase of active sites available for the catalytic reaction. To evaluate the superior activity for e-NRR of the electrode loaded with 1mM $FeCl_3$ chronoamperometry test was performed at different voltages in the range between -0.31 and -0.47 V vs RHE. Ar control experiments have been performed at each chronoamperometry. The amount of produced ammonia has been calculated as the difference between the ammonia quantity obtained under Argon flux and the under N_2 flux. Figures 6.10 a and b show

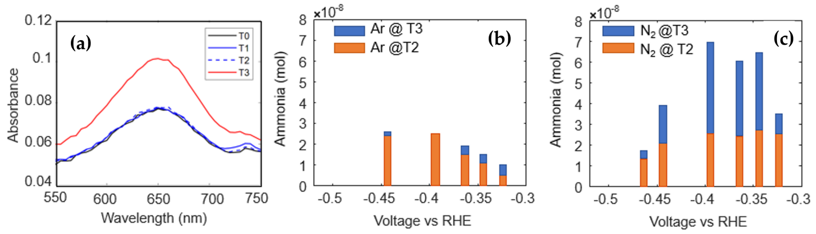

FIGURE 6.10: Experimental procedure adopted for ammonia production estimation: (a) absorbance value in the electrolyte at the beginning (T0), after 10min (T1), after 40min (T2) and after chronoamperometry with N2 flux; (b) Ammonia moles in the cell before (time T0, T1 and T2) and after chronoamperometry (T3) experiments with Ar flux and (c) the corresponding data but with N2.

data about the control experiments. The quantity of ammonia produced under Ar flux at the end of chronoamperometry experiment is negligible compared with the other ones under N_2 flux. In figures 6.11 (a-b) are reported the rates and the faradaic efficiencies of the NRR experiments. The NH_3 yield rate is maximum at -0.35V vs RHE with 26.44 $\mu gmg_{cat}^{-}1h^{-1}$ and a corresponding Faradaic Efficiency of 20.4%. Thanks to the adopted strategy to optimize the morphology and

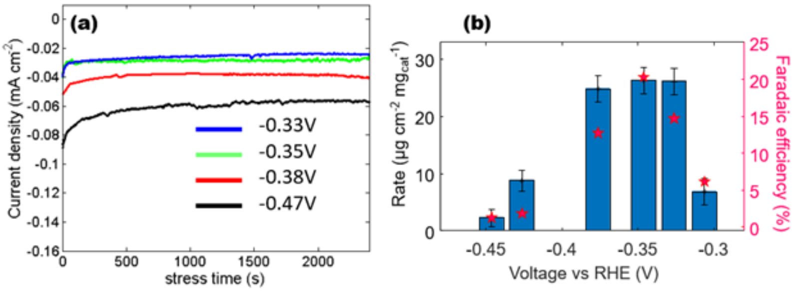

FIGURE 6.11: e-NRR measurements for electrode obtained with 1mM FeCl3 electrode: (a) chronoamperometry results and (b) average NH3 yield rate and Faradaic efficiencies at a given potentials.

improve the catalytic sites by an electrochemical activation process, achieving good results compared to literature. A comparison is reported in Table A.1.

Chapter 7

Conclusions

7.1 Solar mini-module modeling and outdoor tests

As discussed in chapters 3 and 4 the results of outdoor tests performed for 3 days in clear sky conditions on two PV minimodules based on Si HJT technology were quantitatively modeled. Despite the common monitoring close to modules maximum power point the behaviour of the modules was continuously analyzed sweeping the load on the modules from the open to the short circuit condition with a period of about 90 s. This allowed monitoring V_{oc}, maximum power point, I_{sc}, module temperature and the entire I-V curves. Using this approach, a direct comparison between monofacial and bifacial operations within the same Si PV technology was performed, evaluating the quantitative correlation between PV electrical performance, solar irradiance on the PV module front and back, and the module temperature. The results reveal that the observed increase in power output and consequent better energy yield in the case of bifacial operation is mainly due to the higher short circuit current. Furthermore, the high albedo in the afternoon and the high responsivity of the cells to infrared light boost the performances of the bifacial module. The results confirm the effectiveness of bifaciality in improving the power output, proving that this technology plays a crucial role throughout the whole day, both in low and high irradiance conditions. The increase in current is high enough to completely overcome the effect of the higher module temperature and the consequent lower open-circuit voltage observed in bifacial operation. Owing to the experimental data on PV module temperature, the 3D model proposed evaluated the PV system's bifacial gain. The model well reproduces the experimental results of module temperature, V_{oc}, I_{sc}, maximum power point, and energy yield, both in monofacial and bifacial operations.

In summary, the PV module when operated as bifacial exhibits larger temperatures, estimated to be between 9°C and 12 °C, depending on the season, at midday throughout the year for the latitude of Catania. Nevertheless, the bifaciality provides a noticeable advantage in terms of system energy yield. The PV technologies with low αT in absolute value provide more advantages when used in bifacial mode. This is, for example, the case of the SHJ technology used in the experiments here reported, with an αT of 0.26 % °C. From such analysis, the n-type HJT technology appears to be particularly suitable for bifacial photovoltaics given its very low-temperature coefficient and the ability to harvest albedo radiation.

7.2 Solar hydrogen production and ammonia electrosynthesis

The optimization of bifaciality has been studied for a coupled bifacial SHJ PV module PEM-EC system, for solar H_2 production. Optimization was performed by numerical modelling through a 3D model that takes into account several parameters and is well discussed in dedicated chapters. Experimental data show, in good agreement with modelling, that bifaciality, with a 30% average ground albedo, and with no additional equipment, such as lenses, mirrors, etc., provides a boost of STH Efficiency and solar H_2 flux of +13%, concerning the STH efficiency obtained with the monofacial system. The improvement of the produced hydrogen flux can be further increased up to about +22% for a 50% average albedo. The results can be considered a promising starting point for the further development of a larger system in which long-term operation and stability will be tested.

The NRR catalytic properties of Fe-oxide based nanoparticles, obtained by solution-based deposition on carbon cloth electrodes, have been investigated. By electrochemical and structural analyses, a possible improvement for both the ammonia yield rate and the faradaic efficiency with an electrochemical catalyst activation procedure based on a transition from Fe_2O_3 to Fe_3O_4 were demonstrated. The main improvement is related to the nanoparticles' morphology and their modification via cyclovoltammetry activation cycles, which caused an increase of catalyst sites because of the enhancement formation of oxygen vacancies. Catalysts covered with nanoparticles exhibit high electrochemical active area and showed excellent activity for nitrogen reduction reaction, with a faradaic efficiency of 15% and a maximum ammonia production rate of $85 \mu g m g_{cat}^{-1} h^{-1}$

Appendix A

Others tables and figures

A.1

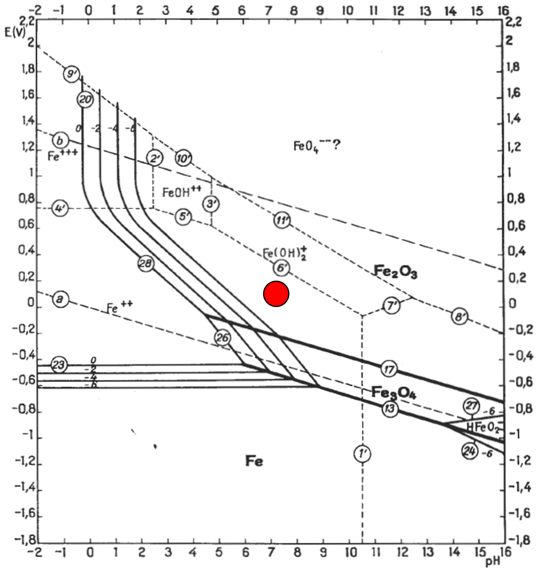

FIGURE A.1: Potential-pH equilibrium diagram for the system iron-water at 25°C. The red circle represents the operative condition.

TABLE A.1: Comparison of results already present in the literature.

Catalyst	**Electrolyte**	**Rate** $\mu g cm^{-2} h^{-1}$	**FE (%)**	**Ref.**
Fe_3O_4/Fe_2O_3	0.01 M PBS	5.5	3.8	This work
Fe_3O_4/Fe_2O_3	0.01 M PBS	26.44	20.4	This work
Fe/Fe_3O_4	0.10 M PBS	/	8.29	[113]
p-Fe_2O_3	0.10 M Na_2SO_4	13.56	7.69	[132]
Fe_2O_3	0.10 M Na_2SO_4	15.9	0.94	[133]
Fe-NPC	0.10 M NaOH	4.46	5.3	[134]
Fe_2O_3 NPS	0.10 M Na_2SO_4	20	3.5	[135]
Fe_3O_4@rGO	0.10 M Na_2SO_4	28.01	11.47	[136]
MFe_3O_4 NPS	0.10 M Na_2SO_4	12.09	16.9	[137]
MFe_3O_4 /Ti	0.10 M Na_2SO_4	/	2.6	[114]

Bibliography

1. Shukla, P. *et al.* Climate Change 2022: Mitigation of Climate Change. *Group III to the Sixth Assessment Report of the Intergovernmental Panel on Climate Change* (2022).
2. Ritchie, H., Roser, M. & Rosado, P. CO2 and Greenhouse Gas Emissions. *Our World in Data.* https://ourworldindata.org/co2-and-other-greenhouse-gas-emissions (2020).
3. Twidell, J. *Renewable energy resources* (Routledge, 2021).
4. Bojek, P. Solar PV Tracking report — September 2022. *Available online: https://www.iea.org/reports/solar-pv.*
5. Group, S. P. *et al.* International technology roadmap for photovoltaic. *Available online: https://itrpv.vdma.org/en/.*
6. Langels, H. & Gannedahl, F. *BiFacial PV Systems: A technological and financial comparison between BiFacial and standard PV panels.* 2018.
7. Liang, T. S. *et al.* A review of crystalline silicon bifacial photovoltaic performance characterisation and simulation. *Energy & Environmental Science* **12,** 116–148 (2019).
8. Gu, W., Ma, T., Ahmed, S., Zhang, Y. & Peng, J. A comprehensive review and outlook of bifacial photovoltaic (bPV) technology. *Energy Conversion and Management* **223,** 113283 (2020).
9. Patel, M. T. *et al.* Temperature-dependent energy gain of bifacial PV farms: A global perspective. *Applied Energy* **276,** 115405 (2020).
10. Yu, B. *et al.* A study on electrical performance of N-type bifacial PV modules. *Solar Energy* **137,** 129–133 (2016).
11. Newborough, M. & Cooley, G. Developments in the global hydrogen market: The spectrum of hydrogen colours. *Fuel Cells Bulletin* **2020,** 16–22 (2020).

12. Detz, R., Reek, J. & Van Der Zwaan, B. The future of solar fuels: when could they become competitive? *Energy & Environmental Science* **11,** 1653–1669 (2018).
13. Bauer, C *et al.* Electricity storage and hydrogen: Technologies costs and environmental burdens. *Tech. Rep.* (2021).
14. Terlouw, T., Bauer, C., McKenna, R. & Mazzotti, M. Large-scale hydrogen production via water electrolysis: a techno-economic and environmental assessment. *Energy & Environmental Science* **15,** 3583–3602 (2022).
15. Wu, S., Salmon, N., Li, M. M.-J., Bañares-Alcántara, R. & Tsang, S. C. E. Energy Decarbonization via Green H2 or NH3? *ACS Energy Letters* **7,** 1021–1033 (2022).
16. Nagaoka, K. *et al.* Carbon-free H2 production from ammonia triggered at room temperature with an acidic RuO2/γ-Al2O3 catalyst. *Science advances* **3,** e1602747 (2017).
17. Eller, K, Henkes, E, Rossbacher, R, Höke, H & Appl, M. Ammonia. *Ullmann's Encyclopedia of Industrial Chemistry,* 647–698 (2012).
18. Bicer, Y., Dincer, I., Zamfirescu, C., Vezina, G. & Raso, F. Comparative life cycle assessment of various ammonia production methods. *Journal of Cleaner Production* **135,** 1379–1395 (2016).
19. Ormerod, R. M. Solid oxide fuel cells. *Chemical Society Reviews* **32,** 17–28 (2003).
20. Lan, R. & Tao, S. Ammonia as a suitable fuel for fuel cells. *Frontiers in energy research* **2,** 35 (2014).
21. Kirubakaran, A., Jain, S. & Nema, R. A review on fuel cell technologies and power electronic interface. *Renewable and sustainable energy reviews* **13,** 2430–2440 (2009).
22. Würfel, P. & Würfel, U. *Physics of solar cells: from basic principles to advanced concepts* (John Wiley & Sons, 2016).
23. Shockley, W. & Queisser, H. J. Detailed balance limit of efficiency of p-n junction solar cells. *Journal of applied physics* **32,** 510–519 (1961).
24. Luque, A. & Hegedus, S. *Handbook of photovoltaic science and engineering* (John Wiley & Sons, 2011).

25. Tanaka, M. *et al.* Development of new a-Si/c-Si heterojunction solar cells: ACJ-HIT (artificially constructed junction-heterojunction with intrinsic thin-layer). *Japanese Journal of Applied Physics* **31,** 3518 (1992).
26. Masuko, K. *et al.* Achievement of more than 25% conversion efficiency with crystalline silicon heterojunction solar cell. *IEEE Journal of Photovoltaics* **4,** 1433–1435 (2014).
27. Sawada, T. *et al. High-efficiency a-Si/c-Si heterojunction solar cell* in *Proceedings of 1994 IEEE 1st World Conference on Photovoltaic Energy Conversion-WCPEC (A Joint Conference of PVSC, PVSEC and PSEC)* **2** (1994), 1219–1226.
28. Mishima, T., Taguchi, M., Sakata, H. & Maruyama, E. Development status of high-efficiency HIT solar cells. *Solar Energy Materials and Solar Cells* **95,** 18–21 (2011).
29. Zhong, C.-l., Geng, K.-w., Luo, L.-e. & Yang, D.-w. An analytical model to explore open-circuit voltage of a-Si: H/c-Si heterojunction solar cells. *Journal of Central South University* **23,** 598–603 (2016).
30. Fujishima, A. & Honda, K. Electrochemical photolysis of water at a semiconductor electrode. *nature* **238,** 37–38 (1972).
31. Kim, D., Sakimoto, K. K., Hong, D. & Yang, P. Artificial photosynthesis for sustainable fuel and chemical production. *Angewandte Chemie International Edition* **54,** 3259–3266 (2015).
32. Walter, M. G. *et al.* Solar water splitting cells. *Chemical reviews* **110,** 6446–6473 (2010).
33. Pagliaro, M. & Konstandopoulos, A. G. *Solar hydrogen: fuel of the future* (Royal Society of Chemistry, 2012).
34. Vielstich, W., Lamm, A. & Gasteiger, H. Handbook of fuel cells. Fundamentals, technology, applications (2003).
35. Parsons, R. The rate of electrolytic hydrogen evolution and the heat of adsorption of hydrogen. *Transactions of the Faraday Society* **54,** 1053–1063 (1958).
36. Greeley, J *et al.* Alloys of platinum and early transition metals as oxygen reduction electrocatalysts. *Nature chemistry* **1,** 552–556 (2009).

37. Laursen, A. B., Kegnæs, S., Dahl, S. & Chorkendorff, I. Molybdenum sulfides—efficient and viable materials for electro-and photoelectrocatalytic hydrogen evolution. *Energy & Environmental Science* **5,** 5577–5591 (2012).
38. Jaramillo, T. F. *et al.* Identification of active edge sites for electrochemical H2 evolution from MoS2 nanocatalysts. *science* **317,** 100–102 (2007).
39. Juangsa, F. B., Irhamna, A. R. & Aziz, M. Production of ammonia as potential hydrogen carrier: Review on thermochemical and electrochemical processes. *International Journal of Hydrogen Energy* **46,** 14455–14477 (2021).
40. Kordali, V, Kyriacou, G. & Lambrou, C. Electrochemical synthesis of ammonia at atmospheric pressure and low temperature in a solid polymer electrolyte cell. *Chemical Communications,* 1673–1674 (2000).
41. Jia, H.-P. & Quadrelli, E. A. Mechanistic aspects of dinitrogen cleavage and hydrogenation to produce ammonia in catalysis and organometallic chemistry: relevance of metal hydride bonds and dihydrogen. *Chemical Society Reviews* **43,** 547–564 (2014).
42. Montoya, J. H., Tsai, C., Vojvodic, A. & Nørskov, J. K. The challenge of electrochemical ammonia synthesis: a new perspective on the role of nitrogen scaling relations. *ChemSusChem* **8,** 2180–2186 (2015).
43. Lv, C. *et al.* Boosting electrocatalytic ammonia production through mimicking "π back-donation". *Chem* **6,** 2690–2702 (2020).
44. Jiao, Y., Zheng, Y., Davey, K. & Qiao, S.-Z. Activity origin and catalyst design principles for electrocatalytic hydrogen evolution on heteroatom-doped graphene. *Nature Energy* **1,** 1–9 (2016).
45. Chen, J. G. *et al.* Beyond fossil fuel–driven nitrogen transformations. *Science* **360,** eaar6611 (2018).
46. Yusufoglu, U. A. *et al.* Simulation of energy production by bifacial modules with revision of ground reflection. *Energy Procedia* **55,** 389–395 (2014).
47. Yusufoglu, U. A. *et al.* Analysis of the annual performance of bifacial modules and optimization methods. *IEEE Journal of Photovoltaics* **5,** 320–328 (2014).

48. Shoukry, I., Libal, J., Kopecek, R., Wefringhaus, E. & Werner, J. Modelling of bifacial gain for stand-alone and in-field installed bifacial PV modules. *Energy Procedia* **92,** 600–608 (2016).
49. Sun, X., Khan, M. R., Deline, C. & Alam, M. A. Optimization and performance of bifacial solar modules: A global perspective. *Applied energy* **212,** 1601–1610 (2018).
50. Lamers, M. *et al.* Temperature effects of bifacial modules: Hotter or cooler? *Solar Energy Materials and Solar Cells* **185,** 192–197 (2018).
51. Zhang, Z. *et al.* The mathematical and experimental analysis on the steady-state operating temperature of bifacial photovoltaic modules. *Renewable energy* **155,** 658–668 (2020).
52. Rodríguez-Gallegos, C. D. *et al.* Monofacial vs bifacial Si-based PV modules: Which one is more cost-effective? *Solar Energy* **176,** 412–438 (2018).
53. McIntosh, K. R., Jung, J., Abbott, M. D. & Sudbury, B. A. *Determination and evaluation of a backsheet's intrinsic reflectance* in *AIP Conference Proceedings* **1999** (2018), 020018.
54. Galluzzo, F. R., Canino, A., Gerardi, C. & Lombardo, S. A. *A new model for predicting bifacial PV modules performance: First validation results* in *2019 IEEE 46th Photovoltaic Specialists Conference (PVSC)* (2019), 1293–1297.
55. Privitera, S. *et al.* Highly efficient solar hydrogen production through the use of bifacial photovoltaics and membrane electrolysis. *Journal of power sources* **473,** 228619 (2020).
56. Notton, G., Cristofari, C., Mattei, M. & Poggi, P. Modelling of a double-glass photovoltaic module using finite differences. *Applied thermal engineering* **25,** 2854–2877 (2005).
57. Ricco Galluzzo, F. *et al.* Numerical modeling of bifacial PV string performance: Perimeter effect and influence of uniaxial solar trackers. *Energies* **13,** 869 (2020).
58. Marion, B. *et al.* *A practical irradiance model for bifacial PV modules* in *2017 IEEE 44th Photovoltaic Specialist Conference (PVSC)* (2017), 1537–1542.

59. Refrigerating. *ASHRAE Handbook, 1985 Fundamentals: An Instrument of Service Prepared for the Profession Containing Technical Information......* (American Society of Heating, Refrigerating and Air-Conditioning Engineers, 1985).
60. Atlas, G. W. Available online: https://globalwindatlas. info/area. *Kuwait (accessed on 12 October 2021)* (2021).
61. Liu, B & Jordan, R. Daily insolation on surfaces tilted towards equator. *ASHRAE J.;(United States)* **10** (1961).
62. Ross Jr, R. *Interface design considerations for terrestrial solar cell modules* in *12th Photovoltaic specialists conference* (1976), 801–806.
63. Xiao, W., Dunford, W. G. & Capel, A. *A novel modeling method for photovoltaic cells* in *2004 IEEE 35th Annual Power Electronics Specialists Conference (IEEE Cat. No. 04CH37551)* **3** (2004), 1950–1956.
64. Santiago, I, Trillo-Montero, D, Moreno-Garcia, I., Pallarés-López, V & Luna-Rodríguez, J. Modeling of photovoltaic cell temperature losses: A review and a practice case in South Spain. *Renewable and Sustainable Energy Reviews* **90,** 70–89 (2018).
65. underground, W. `https://www.wunderground.com/` (2021).
66. Zouine, M *et al. Mathematical models calculating PV module temperature using weather data: Experimental study* in *International Conference on Electronic Engineering and Renewable Energy* (2018), 630–639.
67. Foti, M. *et al. Silicon Heterojunction Solar Module using Shingle interconnection* in *2021 IEEE 48th Photovoltaic Specialists Conference (PVSC)* (2021), 1092–1095.
68. Green, M. *et al.* Solar cell efficiency tables (version 57). *Progress in photovoltaics: research and applications* **29,** 3–15 (2021).
69. Park, H., Chang, S., Park, S. & Kim, W. K. Outdoor performance test of bifacial n-type silicon photovoltaic modules. *Sustainability* **11,** 6234 (2019).
70. Molin, E., Stridh, B., Molin, A. & Wäckelgård, E. Experimental yield study of bifacial PV modules in nordic conditions. *IEEE Journal of Photovoltaics* **8,** 1457–1463 (2018).

71. Jang, J. & Lee, K. Practical performance analysis of a bifacial PV module and system. *Energies* **13,** 4389 (2020).

72. Gu, W. *et al.* Experimental investigation of the bifacial photovoltaic module under real conditions. *Renewable Energy* **173,** 1111–1122 (2021).

73. Abotaleb, A & Abdallah, A. Performance of bifacial-silicon heterojunction modules under desert environment. *Renewable Energy* **127,** 94–101 (2018).

74. Jia, J. *et al.* Solar water splitting by photovoltaic-electrolysis with a solar-to-hydrogen efficiency over 30%. *Nature communications* **7,** 1–6 (2016).

75. Peharz, G., Dimroth, F. & Wittstadt, U. Solar hydrogen production by water splitting with a conversion efficiency of 18%. *International Journal of Hydrogen Energy* **32,** 3248–3252 (2007).

76. Fallisch, A. *et al.* Hydrogen concentrator demonstrator module with 19.8% solar-to-hydrogen conversion efficiency according to the higher heating value. *International Journal of Hydrogen Energy* **42,** 26804–26815 (2017).

77. Nakamura, A. *et al.* A 24.4% solar to hydrogen energy conversion efficiency by combining concentrator photovoltaic modules and electrochemical cells. *Applied Physics Express* **8,** 107101 (2015).

78. Ager, J. W., Shaner, M. R., Walczak, K. A., Sharp, I. D. & Ardo, S. Experimental demonstrations of spontaneous, solar-driven photoelectrochemical water splitting. *Energy & Environmental Science* **8,** 2811–2824 (2015).

79. Cox, C. R., Lee, J. Z., Nocera, D. G. & Buonassisi, T. Ten-percent solar-to-fuel conversion with nonprecious materials. *Proceedings of the National Academy of Sciences* **111,** 14057–14061 (2014).

80. Schüttauf, J.-W. *et al.* Solar-to-hydrogen production at 14.2% efficiency with silicon photovoltaics and earth-abundant electrocatalysts. *Journal of The Electrochemical Society* **163,** F1177 (2016).

81. Kim, J. H., Hansora, D., Sharma, P., Jang, J.-W. & Lee, J. S. Toward practical solar hydrogen production–an artificial photosynthetic leaf-to-farm challenge. *Chemical Society Reviews* **48,** 1908–1971 (2019).

82. Appelbaum, J. Bifacial photovoltaic panels field. *Renewable Energy* **85,** 338–343 (2016).

83. Hansen, C., Riley, D., Deline, C., Toor, F. & Stein, J. *A Detailed Performance Model for Bifacial PV Modules.* tech. rep. (Sandia National Lab.(SNL-NM), Albuquerque, NM (United States), 2017).

84. Deline, C. *et al.* Assessment of bifacial photovoltaic module power rating methodologies—inside and out. *IEEE Journal of photovoltaics* **7,** 575–580 (2017).

85. Chudinzow, D., Haas, J., Díaz-Ferrán, G., Moreno-Leiva, S. & Eltrop, L. Simulating the energy yield of a bifacial photovoltaic power plant. *Solar Energy* **183,** 812–822 (2019).

86. Tjarks, G. *et al.* Energetically-optimal PEM electrolyzer pressure in power-to-gas plants. *Applied energy* **218,** 192–198 (2018).

87. Jain, D. & Lalwani, M. A review on optimal inclination angles for solar arrays. *International Journal of Renewable Energy Research (IJRER)* **7,** 1053–1061 (2017).

88. Ghavam, S., Vahdati, M., Wilson, I. & Styring, P. Sustainable ammonia production processes. *Frontiers in Energy Research,* 34 (2021).

89. Bicer, Y. & Dincer, I. Life cycle assessment of ammonia utilization in city transportation and power generation. *Journal of cleaner production* **170,** 1594–1601 (2018).

90. Dolan, R. H., Anderson, J. E. & Wallington, T. J. Outlook for ammonia as a sustainable transportation fuel. *Sustainable Energy & Fuels* **5,** 4830–4841 (2021).

91. Smith, C., Hill, A. K. & Torrente-Murciano, L. Current and future role of Haber–Bosch ammonia in a carbon-free energy landscape. *Energy & Environmental Science* **13,** 331–344 (2020).

92. Fernandez, C. A. & Hatzell, M. C. Editors' Choice—Economic Considerations for Low-Temperature Electrochemical Ammonia Production: Achieving Haber-Bosch Parity. *Journal of The Electrochemical Society* **167,** 143504 (2020).

93. Faria, J. A. Renaissance of ammonia synthesis for sustainable production of energy and fertilizers. *Current Opinion in Green and Sustainable Chemistry* **29,** 100466 (2021).

94. Liu, A. *et al.* Two-dimensional CuAg/Ti 3 C 2 catalyst for electrochemical synthesis of ammonia under ambient conditions: a combined experimental and theoretical study. *Sustainable Energy & Fuels* **4,** 5061–5071 (2020).
95. Tang, C. & Qiao, S.-Z. How to explore ambient electrocatalytic nitrogen reduction reliably and insightfully. *Chemical Society Reviews* **48,** 3166–3180 (2019).
96. Liu, D. *et al.* Development of electrocatalysts for efficient nitrogen reduction reaction under ambient condition. *Advanced Functional Materials* **31,** 2008983 (2021).
97. Skulason, E. *et al.* A theoretical evaluation of possible transition metal electro-catalysts for N 2 reduction. *Physical Chemistry Chemical Physics* **14,** 1235–1245 (2012).
98. Yang, X. *et al.* Defect-induced Ce-doped Bi2WO6 for efficient electrocatalytic N2 reduction. *ACS Applied Materials & Interfaces* **13,** 19864–19872 (2021).
99. Majumder, M. *et al.* Rational design of graphene derivatives for electrochemical reduction of nitrogen to ammonia. *ACS nano* **15,** 17275–17298 (2021).
100. Wang, B., Huang, S., Yang, L., Fu, Q. & Bu, Y. Regulating the Catalytic Performance of a Dual-Atom Iron Species Deposited on Graphitic Carbon Nitride for Electrochemical Nitrogen Reduction. *The Journal of Physical Chemistry C* **125,** 14253–14262 (2021).
101. Song, P., Kang, L., Wang, H., Guo, R. & Wang, R. Nitrogen (N), phosphorus (P)-codoped porous carbon as a metal-free electrocatalyst for N2 reduction under ambient conditions. *ACS applied materials & interfaces* **11,** 12408–12414 (2019).
102. Feng, J. & Pan, H. Electronic state optimization for electrochemical N 2 reduction reaction in aqueous solution. *Journal of Materials Chemistry A* **8,** 13896–13915 (2020).
103. Wang, H. *et al.* Amorphous sulfur decorated gold nanowires as efficient electrocatalysts toward ambient ammonia synthesis. *ACS Sustainable Chemistry & Engineering* **7,** 19969–19974 (2019).

104. Shi, M.-M. *et al.* Au sub-nanoclusters on TiO2 toward highly efficient and selective electrocatalyst for N2 conversion to NH3 at ambient conditions. *Advanced Materials* **29,** 1606550 (2017).

105. Wang, H. *et al.* Electrochemical fabrication of porous Au film on Ni foam for nitrogen reduction to ammonia. *Small* **15,** 1804769 (2019).

106. Qin, Q., Heil, T., Antonietti, M. & Oschatz, M. Single-site gold catalysts on hierarchical N-doped porous noble carbon for enhanced electrochemical reduction of nitrogen. *Small Methods* **2,** 1800202 (2018).

107. Xu, Y. *et al.* Anchoring Au nanoparticles on Bi ultrathin nanosheets for use as an efficient heterogeneous catalyst for ambient-condition electrochemical ammonia synthesis. *Sustainable Energy & Fuels* **4,** 4516–4521 (2020).

108. Liu, C. *et al.* Ambient N 2-to-NH 3 fixation over a CeO 2 nanoparticle decorated three-dimensional carbon skeleton. *Sustainable Energy & Fuels* **6,** 3344–3348 (2022).

109. Ying, H. *et al.* Regeneration of porous Fe3O4 nanosheets from deep eutectic solvent for high-performance electrocatalytic nitrogen reduction. *Journal of Colloid and Interface Science* **602,** 64–72 (2021).

110. Cui, B. *et al.* Electrochemical synthesis of ammonia directly from N 2 and water over iron-based catalysts supported on activated carbon. *Green Chemistry* **19,** 298–304 (2017).

111. Geng, C., Li, J., Weiske, T. & Schwarz, H. Complete cleavage of the N≡ N triple bond by Ta2N+ via degenerate ligand exchange at ambient temperature: A perfect catalytic cycle. *Proceedings of the National Academy of Sciences* **116,** 21416–21420 (2019).

112. Ertl, G. Surface science and catalysis—studies on the mechanism of ammonia synthesis: the PH Emmett award address. *Catalysis Reviews Science and Engineering* **21,** 201–223 (1980).

113. Hu, L. *et al.* Ambient electrochemical ammonia synthesis with high selectivity on Fe/Fe oxide catalyst. *ACS Catalysis* **8,** 9312–9319 (2018).

114. Liu, Q. *et al.* Ambient N 2 fixation to NH 3 electrocatalyzed by a spinel Fe 3 O 4 nanorod. *Nanoscale* **10,** 14386–14389 (2018).

115. Lü, F. *et al.* Nitrogen-coordinated single Fe sites for efficient electrocatalytic N2 fixation in neutral media. *Nano Energy* **61,** 420–427 (2019).

116. Licht, S. *et al.* Ammonia synthesis by N2 and steam electrolysis in molten hydroxide suspensions of nanoscale Fe2O3. *Science* **345,** 637–640 (2014).

117. Andersen, S. Z. *et al.* A rigorous electrochemical ammonia synthesis protocol with quantitative isotope measurements. *Nature* **570,** 504–508 (2019).

118. Cui, X. *et al.* Highly selective electrochemical reduction of dinitrogen to ammonia at ambient temperature and pressure over iron oxide catalysts. *Chemistry–A European Journal* **24,** 18494–18501 (2018).

119. Liu, H., Guijarro, N. & Luo, J. The pitfalls in electrocatalytic nitrogen reduction for ammonia synthesis. *Journal of Energy Chemistry* **61,** 149–154 (2021).

120. Leonardi, M. *et al.* Role of the Membrane Transport Mechanism in Electrochemical Nitrogen Reduction Experiments. *Membranes* **12,** 969 (2022).

121. Li, L., Tang, C., Yao, D., Zheng, Y. & Qiao, S.-Z. Electrochemical nitrogen reduction: identification and elimination of contamination in electrolyte. *ACS Energy Letters* **4,** 2111–2116 (2019).

122. Zhao, Y. *et al.* Ammonia detection methods in photocatalytic and electrocatalytic experiments: how to improve the reliability of NH3 production rates? *Advanced Science* **6,** 1802109 (2019).

123. Milazzo, R. G. *et al.* Ultralow loading electroless deposition of IrOx on nickel foam for efficient and stable water oxidation catalysis. *International Journal of Hydrogen Energy* **45,** 26583–26594 (2020).

124. Almeida, T. P. *et al.* Visualized effect of oxidation on magnetic recording fidelity in pseudo-single-domain magnetite particles. *Nature Communications* **5,** 1–6 (2014).

125. Tzitzios, V. *et al.* Large-scale synthesis, size control, and anisotropic growth of &gamma-Fe2O3 nanoparticles: Organosols and hydrosols. *Journal of Nanoscience and Nanotechnology* **7,** 2753–2757 (2007).

126. Iyengar, S. J. *et al.* Colloidal properties of water dispersible magnetite nanoparticles by photon correlation spectroscopy. *RSC advances* **6,** 14393–14402 (2016).

127. Yamashita, T. & Hayes, P. Analysis of XPS spectra of Fe2+ and Fe3+ ions in oxide materials. *Applied surface science* **254,** 2441–2449 (2008).

128. Poulin, S, França, R, Moreau-Bélanger, L & Sacher, E. Confirmation of X-ray photoelectron spectroscopy peak attributions of nanoparticulate iron oxides, using symmetric peak component line shapes. *The Journal of Physical Chemistry C* **114,** 10711–10718 (2010).

129. Sang, Y. *et al.* Constructing oxygen vacancy-enriched Fe 2 O 3@ NiO heterojunctions for highly efficient electrocatalytic alkaline water splitting. *CrystEngComm* **24,** 199–207 (2022).

130. Perry, S. *et al.* Pourbaix diagrams as a simple route to first principles corrosion simulation. *Journal of The Electrochemical Society* **166,** C3186 (2019).

131. Beverskog, B & Puigdomenech, I. Revised pourbaix diagrams for iron at 25–300 C. *Corrosion Science* **38,** 2121–2135 (1996).

132. Wang, Z. *et al.* Electrocatalytic nitrogen reduction to ammonia by Fe2O3 nanorod array on carbon cloth. *ACS Sustainable Chemistry & Engineering* **7,** 11754–11759 (2019).

133. Xiang, X., Wang, Z., Shi, X., Fan, M. & Sun, X. Ammonia synthesis from electrocatalytic N2 reduction under ambient conditions by Fe2O3 nanorods. *ChemCatChem* **10,** 4530–4535 (2018).

134. Song, P. *et al.* Ambient electrochemical N2 reduction to NH3 on nitrogen and phosphorus co-doped porous carbon with trace iron in alkaline electrolytes. *ChemElectroChem* **7,** 212–216 (2020).

135. Wang, M., Li, F. & Liu, J. Glycerine-based synthesis of a highly efficient Fe 2 O 3 electrocatalyst for N 2 fixation. *RSC advances* **10,** 29575–29579 (2020).

136. Wang, F. *et al.* Nano-Ferric Oxide Embedded in Graphene Oxide: High-performance Electrocatalyst for Nitrogen Reduction at Ambient Condition. *Energy & Environmental Materials* **4,** 88–94 (2021).
137. He, X. *et al.* Facile electrochemical fabrication of magnetic Fe3O4 for electrocatalytic synthesis of ammonia used for hydrogen storage application. *International Journal of Hydrogen Energy* **46,** 24128–24134 (2021).